Lehrstuhl für THERMODYNAMIK

BACHELOR'S THESIS

Quantification of Acoustic Driving Rates in Gas Turbine Combustion Chambers

Autor:
Francisco García Villanueva

Matrikel-No:
03699470

Betreuer:
Prof. Dr.-Ing. Thomas Sattelmayer
Thomas Hofmeister, M.Sc.

September 5, 2018

Lehrstuhl für Thermodynamik
Prof. Dr.-Ing. Thomas Sattelmayer

Erklärung

Hiermit versichere ich, die vorliegende Arbeit selbstständig verfasst zu haben. Ich habe keine anderen Quellen und Hilfsmittel als die angegebenen verwendet.

Ort, Datum	Francisco García Villanueva

Contents

Abstract

This Bachelor's thesis presents a numerical method for the quantification of the acoustic driving rate in non-compact thermoacoustic systems. The drop of the compactness assumption in the High Frequency (HF) acoustic range presents a challenge since the spatial distribution of the oscillating heat release rate is not negligible. The employed Source Term Function (STF) enables to couple the fluctuating heat release rate with the acoustic velocity and pressure of the Linearised Helmholtz Equations (LHE). The implementation of this STF as a part of a Finite Element Method (FEM) requires the mean temperature and the mean heat release rate fields. These mean fields are extracted by means of a reactive Computational Fluid Dynamics (CFD) simulation using an extended version of the Flamelet Generated Manifold (FGM), which accounts for heat and stretch losses. The reactive CFD constitutes the main part of this thesis and it aims for replacing experimentation as the source of the needed mean fields. In order to prove the suitability of the FGM extended model to reproduce the flame behaviour, linear stability analysis with both CFD and experimental flame images are conducted. The comparison of them shows the capability of the numerical method with a reactive CFD simulation to predict thermoacoustic instabilities.

Nomenclature

Roman Symbols

A	Area	$\left[m^2\right]$
c	Speed of Sound	$\left[\frac{m}{s}\right]$
e	Internal Energy	$\left[\frac{W}{m^3}\right]$
f	Frequency	$\left[\frac{rad}{s}\right]$
H_i	Fuel Lower Specific Value	$\left[\frac{kJ}{kg}\right]$
He	Helmholtz number	$[-]$
I	Local Formation Rate	$\left[\frac{rad}{s}\right]$
J_m	m-th Bessel Function	$[-]$
Ka	Karlovitz Number	$[-]$
l	Characteristic length	$[m]$
$\dot{m}$	Mass Flow Rate	$\left[\frac{kg}{s}\right]$
Ma	Mach Number	$[-]$
$\mathcal{O}$	Order of Magnitude	$[-]$
p	Pressure	$[Pa]$
q	Heat Release Rate	$\left[\frac{W}{m^3}\right]$
Q_{th}	Total Combustion Heat	$[W]$
R	Air Constant	$\left[\frac{J}{kg\,K}\right]$
Re	Reynolds Number	$[-]$
t	Time	$[s]$
T	Temperature	$[K]$
$\mathbf{u}$	Velocity vector	$\left[\frac{m}{s}\right]$
$\mathbf{x}$	Coordinates	$[m]$
Z	Acoustic Impedance	$\left[\frac{kg}{m\,s}\right]$

Greek Symbols

ρ	Density	$\left[\frac{kg}{m^3}\right]$
κ	Ratio of Specific Heats	$[-]$
π	Number pi	$[-]$
λ	Excess air	$\left[\frac{kg_{air}}{kg_{air,stch}}\right]$
θ	Azimuthal Coordinate	$[rad]$

ν	Growth Rate	$\left[\frac{rad}{s}\right]$
α	Damping Rate	$\left[\frac{rad}{s}\right]$
β	Driving Rate	$\left[\frac{rad}{s}\right]$
ω	Angular Frequency	$\left[\frac{rad}{s}\right]$
$\overline{\dot{\omega}_c}$	Formation Rate	$\left[\frac{rad}{s}\right]$
$\Delta'(\mathbf{x}, t)$	Acoustic Displacement Field	

Operators

$\frac{\partial()}{\partial()}$	Partial derivative
$\frac{D()}{D()}$	Material Differentiation
$\frac{d()}{d()}$	Total Differentiation
$d()$	Differential form of ()
$\nabla \cdot ()$	Divergence
$\nabla()$	Gradient
$\nabla x()$	Cross Product
$\mathscr{R}()$	Real Part
$\Im()$	Imaginary Part

Subscripts

$()_{ref}$	Reference State
$()_1$	First Transversal Mode
$()_c$	Combustion Chamber

Superscripts

$()'$	Fluctuating in Time Domain
$\overline{()}$	Mean Value
$\dot{()}$	Temporal Rate

Acronyms

HF	High Frequency
LF	Low Frequency
CFD	Computational Fluid Dynamics
FEM	Finite Elements Method
STF	Source Term Function
LHE	Linearised Helmholtz Equations
LEE	Linearised Euler Equations
FTF	Flame Transfer Function

1 Introduction

According to the UN demographic projections [23], the world population will raise up to 8.8 billion people until 2050 in the smallest growth scenario, as shown in Fig. 1.1. Such an increase represents a 14.3 % population enlargement. This increase in the highest growth scenario denotes a 58.3 % gain with respect to the actual population. From these data can be foreseen that the world energy demand will also augment. Indeed, the predictions in [4] estimate a consumption boost from 575 quadrillion ($\cdot 10^{15}$) British thermal units (Btu) in 2015 to 736 quadrillion Btu in 2040, which is roughly a 30 % increase in energy demand. In order to maintain the welfare state assuring a sustainable usage of natural resources, the source of energy must be clean and efficient.

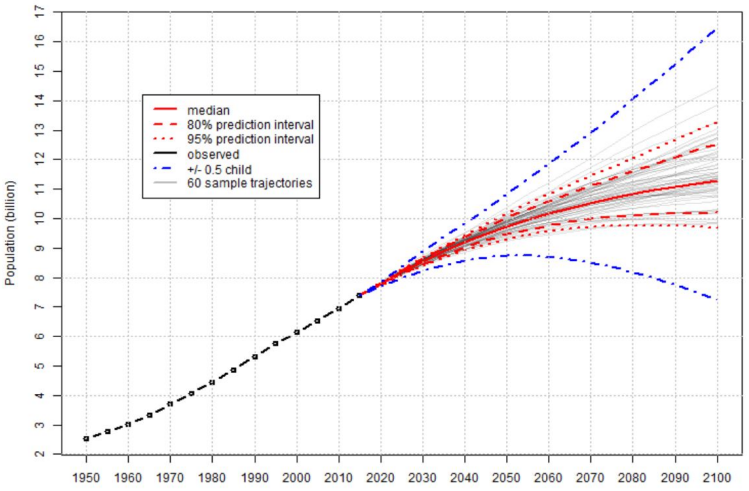

Figure 1.1: World total population forecast [23]

The annual statistical review of world energy from BP shows that the usage of fossil fuels such as coal, oil and natural gas represent almost a 70 % of global consumption [7]. Moreover, from Fig. 1.2 it can be inferred that the source of energy with the strongest current development is natural gas with a raise in 2017 of a 3 %. However, according to [4], in the time lapse from 2015 to 2040 renewable sources of energy are to be the fastest growing. These predictions also forecast interesting trends, such as the stagnation of coal usage and a small loss of energy share by oil, which will still be the biggest contributor (c.f. Fig. 1.2). Natural gas is expected to be the fossil fuel whose use will increase the most almost a 43 %.

This increase in natural gas is constituted by its transportation suitability and environmen-

tal causes: Natural gas burning is the cleanest among fossil fuels as it produces 27.4 % less carbon dioxide (CO_2) emissions than ordinary diesel fuel [5]. CO_2 is the main responsible of greenhouse effect. Besides that,it provokes around 80% less nitrogen dioxide (NO_x) emissions than coal [5]. NO_x release is responsible of acidic rain and damages the ozone cape.

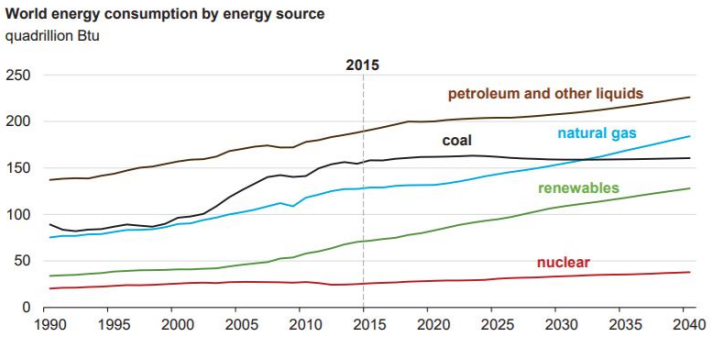

Figure 1.2: World energy consumption predictions by source of energy [4]

Therefore, the importance of natural gas powered turbines is a key factor in the future of energy production [16]. The main commitment of stationary gas turbines is to boost the energy production in those moments when renewable energies are not able to supply enough energy. Those situations can be triggered by weather conditions (i.e. Lack of wind or sun) [28]. The features making them suitable for this co-generation are [26]:

- Their flexible starting-up and shooting-down. The state of the art allows heavy duty gas turbines to reach full power from cold start in less than 7 minutes.
- High thermal efficiency. The current efficiency peaks in combined generation cycles approach 65 %.

Despite this advantages, the NO_x production legislation is tough to accomplish. Therefore, combustion chambers in gas turbines work in lean-premixed conditions as it reduces the emissions, as Fig. 1.3 shows. Lean-premixed combustion involves a fuel-air mixture with an excess air ratio λ with respect to the stoichiometric conditions [9]. In terms of emissions the lean-premixed combustion has more advantages, e.g. reduction of the non-burnt hydrocarbons and also a soot diminution [27].

However, these operating conditions can cause the development of instabilities [1] (e.g. flame blow-off, flashback or thermoacoustic instabilities) [9]. The flame-acoustic interactions can cause self-sustained oscillations. Those fluctuations may lead to an undesired emissions raise due to a variation of the designed thermodynamic properties distribution in the combustion chamber [22]. In extreme cases the instability can cause damage in the combustor chamber because of the pressure oscillations with their corresponding vibrations [9]. To avoid this inconvenience, a restriction on the operational range is forced.

[1] Presented in Chapter 2

This Bachelor's thesis focuses on this thermoacoustic instabilities. The origin of them is the interaction between the unsteady heat release rate and the acoustic modes.

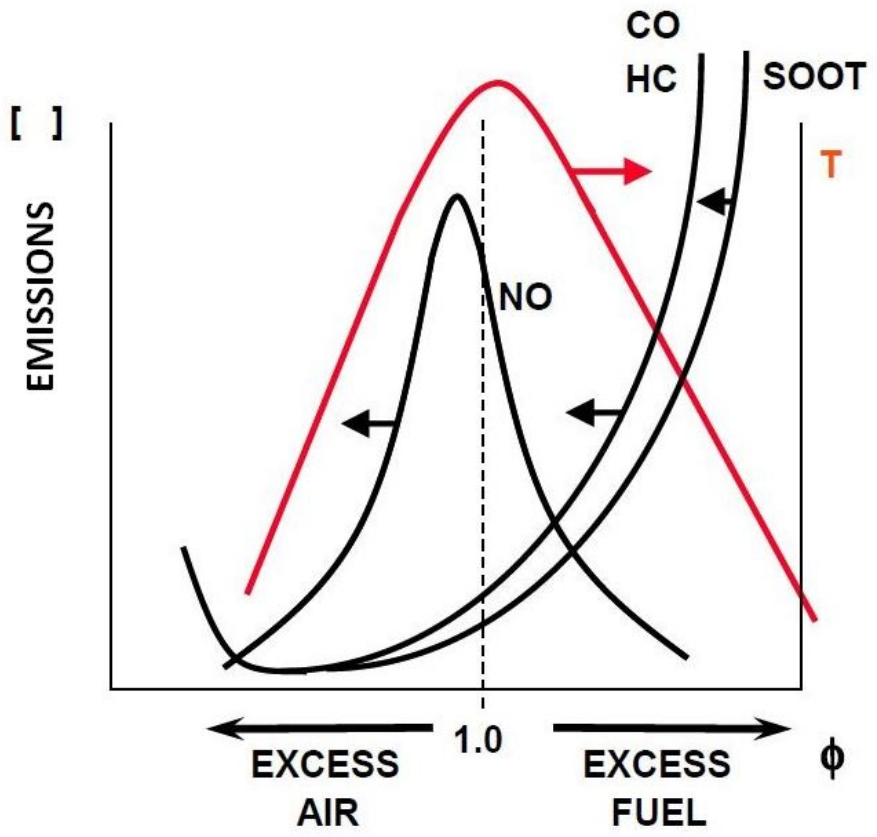

Figure 1.3: Temperarute and emissions in dependence on ϕ [9]

1.1 Motivation and Objectives

The prediction of thermoacoustic instabilities in lean-premixed combustion chambers assures a safe operation, while fulfilling the emission requirements [9]. The compactness assumption simplifies the modelling of the heat release rate fluctuations in the Low Frequency (LF) range [11]. However, in the HF range this assumption is no longer held, so the LF models are not valid [22]. A linear numerical model for HF oscillation which couples the heat release rate fluctuation with the acoustic pressure and velocity fields, was developed by [11]. This STF requires the mean temperature and heat release rate fields to predict the thermoacoustic instabilities in the HF range.

Up to now, the linear stability analysis conducted with this STF used experimental images to extract the mean fields [10]. However, this experimental data is affected by acoustics which is an undesired situation because it compromises the linearity assumption. In order to obtain

mean fields free of acoustic interaction, the implementation of steady-state CFD simulations is motivated. Additionally, a correct CFD implementation allows a cost and time reduction compared to experiments.

Hence, the primary objective of this thesis is to quantify the acoustic driving rates of the first transversal mode using a CFD steady-state simulation. This simulation provides the STF necessary mean temperature and heat release rate fields. The main challenge to reproduce the reaction process in a CFD simulation is the identification of an appropriate combustion model.

Finally, a linear stability analysis using the numerical data is conducted and its results are compared with the experimentally obtained driving rates. In this way, a validation of the numerically assessed thermoacoustic stability prediction is performed.

1.2 Thesis Structure

This thesis is organised in the following way:

- Chapter 2 introduces the instabilities occurring in a lean-premixed combustion system and the state-of-the-art measures to prevent those. It also exposes the criteria used to asses the appearance of thermoacoustic instabilities.
- Chapter 3 provides information about the basic thermoacoustic theory to understand the governing physical phenomena. The STF used to couple the flame-acoustic interaction is explained.
- Chapter 4 explains the CFD procedure that enables the determination of the temperature and heat release rate mean fields.
- Chapter 5 is comprised of the FEM set-up and the results for the numerical linear stability analysis, which is compared with the experimental one.
- Chapter 6 presents a summary of the findings and proposes future work and improvement possibilities.

2 Gas Turbines Instabilities

Lean-premixed combustion may derive into stability issues, which are costly and technically challenging [9]. Additionally, they usually appear in the last design steps when all the combustion chamber elements are coupled since some instabilities are caused by their interactions (e.g. nozzle-nozzle, can-can, etc.). According to [9], those instabilities, causing high oscillation amplitudes inside the combustors, often even appear on the customer's side.

Lean-premixed combustion is specially prone to thermoacoustic instabilities because of the lack of acoustic damping in comparison to other combustion system, i.e. diffusion flame combustors or Rich-Quench-Lean combustors [9]. In the later systems around 70 % of the air enters the combustion chamber through quench holes in the midway. The secondary air introduction introduces strong vortical interaction, so that the energy in the acoustics modes is decreased, resulting in an effective damping effect [22].

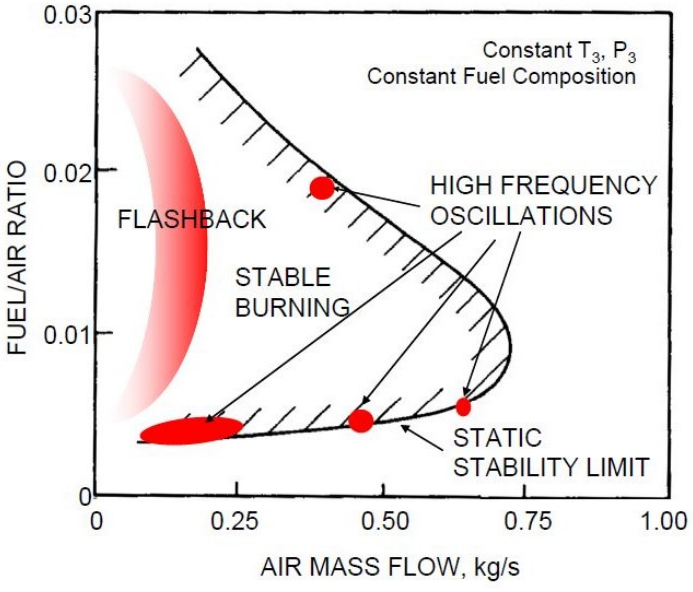

Figure 2.1: Region of instability for a gas turbine combustor at a fixed inlet temperature and pressure [9]

In Fig. 2.1 can be appreciated that for lean mixtures (lower graph boundary) there is a stability limit where HF oscillations appear. This involves that operational points cannot be as

lean as desired in Fig. 1.3, due to the arise of these instabilities. However, in stationary gas turbines the severe emissions legislation motivates designs that operate really close to these potential unstable regions. Other effects come up when trying to further reduce emissions, i.e. “hot wall strategies“. This technique diminishes the acoustic damping even more since it creates less CO by injecting as few cooling air as possible into the chamber. Therefore, industrial stationary gas turbines are more susceptible to suffer from dynamic instabilities, such as HF oscillations [9], [22] and [27].

Besides that, other interesting considerations can be inferred from Fig. 2.1. For instance, when the application requires safety and reliability like aviation gas turbines, designs forsake this low emission approach and go towards richer fuel/air mixtures [29]. On the other hand, flashback is a static instability that refers to the operational range where the flame displaces towards the burner. This phenomena occurs for low mass flows since the laminar flame speed becomes larger than the flow speed. Therefore the burning is produced before the combustion chamber which is an inconvenience and may lead to severe damage in the combustor [17].

The most common flashback avoidance method is known as Swirl-Stabilised combustion, it consists of inducing a tangential velocity to the mean flow in order to avoid flame speeds to be larger than axial velocities even for low mass flows [9] and [17]. This method influences the combustor flow shape, which has a determinative importance in the election of a combustion model for the CFD simulation as it is explained in Chapter 4.

2.1 Thermoacoustic Importance in Combustion Chambers

To understand the reason behind acoustic research in gas turbines, the physical processes occurring with noise propagation must be clarified. Sound waves are defined as mechanical vibrations, whose particles move around a mid-position, which are able to transport energy but not matter and can transport information [18]. Furthermore, these vibrations represent a density fluctuation, caused by an adiabatic compression which means that there is a change in the thermodynamic properties [19].

Therefore, we are mainly interested in the thermodynamic fluctuations inside the combustion chamber and specially the feedback that these acoustic fluctuations give to the flame. We imagine the following procedure: An acoustic wave hits the flame, which causes a change in the flame shape, so that there is a heat release rate variation. This unsteady heat release rate fluctuation act as a source to the acoustic field enhancing the acoustic energy into the system. Amplified acoustic amplitudes can provoke further heat release rate fluctuations so that a self-sustained feedback loop is established. These loop may result fatal for the combustor and designs must avoid the most severe acoustics modes as can lead in an undesirable acoustics-flame coupling.

2.2 Rayleigh's Criterion

A criteria to determine whether these flame-acoustic interaction may lead to an oscillation cycle or not is necessary. This criteria was introduced by J.W.S. Rayleigh in the late 19th century and also known as 'singing flame' [25].

In a thermo-acoustic problem pressure fluctuations and heat release rate variations are coupled. The Rayleigh's criterion determines if the oscillation are self-sustained. For this to occur the net supply of energy due to acoustics exceeds the system damping. According to Rayleigh [25], the resulting work calculated with Eqn. (2.1) must be positive for the oscillations to be self-sustained.

$$W = \frac{1}{T}\oint_0^T p\, dV = \frac{1}{T}\oint_0^T p\, \frac{dV}{dt}\, dt \tag{2.1}$$

In the Eqn. (2.1), also known as Rayleigh's Hydrodynamic Criterion, the term $\frac{dV}{dt}$ represents the rate of volume injection [18]. According to [22], this equation can be re-written for thermo-acoustic probles as:

$$\frac{1}{T}\int_0^T \int_V p'(x,t)\; q'(x,t)\; dV dt > 0 \tag{2.2}$$

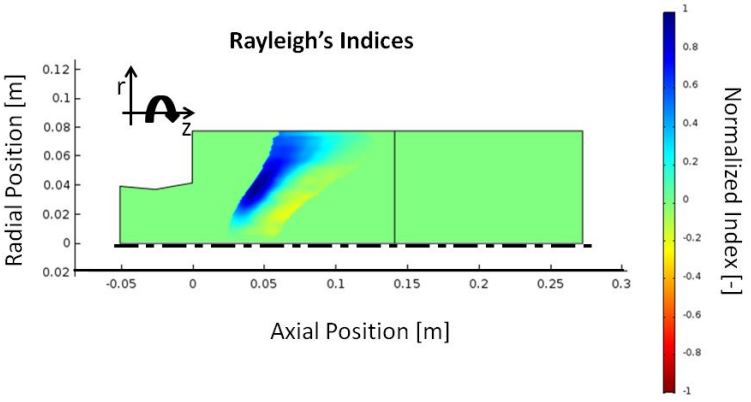

Figure 2.2: Example of the interaction between p' and q' in a combustor chamber

Fig. 2.2 illustrates the application of Eqn. 2.2 in a combustion chamber. The Rayleigh indices are spatially evaluated in Fig. 2.2 and allow to visualize the regions where the flame-acoustic interaction occurs. To assess the stability, the Rayleigh indices are integrated over the complete volume. Fig. 2.3 displays the importance of the phase difference between q' and p' for the oscillation amplitude. If p' and q' are in phase the oscillation amplitude is bigger than when they are separated by 90º.

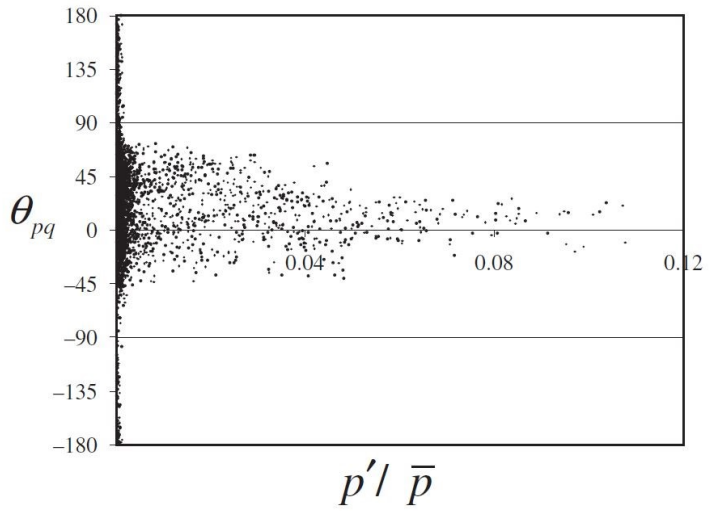

Figure 2.3: Dimensionless pressure oscillation amplitude, depending on the phase difference between the pressure mode and the heat release rate fluctuation [9]

3 Thermoacoustic Fundamentals

In this chapter the fundamental thermoacoustic equations and phenomena are introduced. The objective is to present the set of linearised governing equations, known as Linearised Helmholtz Equations (LHE) in the frequency domain. The first step consist of defining the required assumptions to derive the LHE in the time domain. Then, the concept of a transversal mode is presented. Next, the coupling between heat release rate fluctuations and the acoustic fields is assessed. Finally, the Fourier transforms are applied to work in the frequency domain.

3.1 Derivation of the Helmholtz Equations

Firstly, an important assumption is made: Despite the working fluid is a mixture between fuel and air, the fluid is considered to be just air. This is occurs because the air-to-fuel ratio is high [8]. Therefore, the working fluid is defined by the air constant $R = 287.1 \left[\frac{J}{kg \cdot K}\right]$. The ideal gas law can be used to describe the gas state [6]:

$$p = R\ T\ \rho \tag{3.1}$$

where p is the pressure, T denotes the temperature and ρ the density. The starting point Eqns. for obtaining the LHE are the continuity, momentum and energy Eqns. [18]:

$$\frac{\partial \rho}{\partial t} + \nabla \cdot (\rho\ \mathbf{u}) = 0 \tag{3.2}$$

$$\rho\ \frac{D\mathbf{u}}{Dt} + \nabla \cdot p = 0 \tag{3.3}$$

$$d\rho(p,e) = \left.\frac{\partial \rho}{\partial p}\right|_{de=0} dp + \left.\frac{\partial \rho}{\partial e}\right|_{dp=p} de = \frac{1}{c^2}\ dp + \frac{\overline{\rho}\ (\kappa - 1)}{c^2}\ de \tag{3.4}$$

In these Eqns. **u** represents the velocity vector, c the speed of sound and e denotes the specific internal energy. For the development of Eqn. 3.3 both friction effects and body forces are

neglected. This assumptions make Eqn. 3.3 be known as Euler Equation. After introducing the equations the required linearisation for the STF is performed. To do that, the variables characterised by an oscillation around a mean value are separated into the superposition of the mean value plus the fluctuation around it as it can be seen in Eqn. 3.5 [22]. The fluctuating part ()' averages the mean flow value, but contrary to the mean flow variables, they are time dependent. Additionally, working under the assumption of isentropic acoustics allows to relate the acoustic pressure and density, as it is displayed in Eqn. (3.6) [19].

$$p(\mathbf{x},t) = \overline{p} + p'(\mathbf{x},t) \qquad \mathbf{u}(\mathbf{x},t) = \mathbf{u}'(\mathbf{x},t) \qquad \rho(\mathbf{x},t) = \overline{\rho} + \rho'(\mathbf{x},t) \tag{3.5}$$

$$\rho' = \frac{p'}{\overline{c}^2} \tag{3.6}$$

Assuming that the fluctuation perturbations ()' are small in comparison to the mean flow counterparts $\overline{()}$ (ie.$p' << \overline{p}$, $\rho' << \overline{\rho}$ and $u' << \overline{c}$). It is possible to introduce, neglecting the second order fluctuating terms, Eqn. (3.5) into Eqns. (3.2) and (3.3). Next, density can be replaced using Eqns. (3.4) and (3.6) . And the final result are the Linearised Helmotz Equation (LHE):

$$\frac{\partial p'}{\partial t} + c^2\,\overline{\rho}\,\nabla\cdot\mathbf{u'} = (\kappa-1)\;q' \tag{3.7}$$

$$\overline{\rho}\,\frac{\partial \mathbf{u'}}{\partial t} + \nabla p' = 0 \tag{3.8}$$

According to [19], the internal energy time variation $\frac{de}{dt}$ can excite an acoustic field. In this particular case, the source term in Eqn. (3.7) is the heat release rate fluctuation q', which corresponds to the internal energy time variation. This means that q' is responsible for exiting the acoustic field in the frame of this thesis. The following steps are to determine how to close this term in relationship with the acoustic field.

3.2 Longitudinal and Transversal Acoustics

In this section longitudinal and transversal acoustic modes in cylindrical ducts are introduced. In order to understand the type of pressure mode investigated in this thesis. More information about the longitudinal and transversal pressure modes can be found in [9], [18] or [22].

The starting point is the homogeneous wave Eqn. (3.9). It is derived by calculating the temporal derivative Eqn.(3.7). And then the divergence of Eqn. (3.8) is multiplied per the speed

of sound powered to the squared. Finally, one equation is substracted to the other one.

$$\frac{\partial^2 p'}{\partial t^2} + c^2 \nabla^2 p' = 0 \tag{3.9}$$

Since only the pressure mode distribution is investigated, no source term is added to the wave Eqn.(3.9). This Eqn. permits to infer the pressure mode distribution depending on time and location. The chosen acoustic boundary conditions to solve the Wave Eqn. in terms of pressure at the inlet (x = 0) and outlet (x = L) are seen in Eqn. (3.10). They denote an inlet being a large plenum and an outlet reflecting back all the sound waves:

$$p'(t,0,r,\theta) = 0 \qquad\qquad p'(t,L,r,\theta) = p'_{max} \tag{3.10}$$

Following [9] procedure for the aforementioned boundary conditions in Eqn. (3.10) the pressure distribution is obtained:

$$p'_{l,m,n}(t,x,r,\theta) = \underbrace{J_m\left(\frac{j_{m,n} r}{R}\right)}_{FirstTerm} \cdot \underbrace{\sin\left[\frac{(2l+1)\pi x}{2L}\right]}_{SecondTerm} \cdot \underbrace{\cos(\omega_{l,m,n} t - m\theta)}_{ThirdTerm} \tag{3.11}$$

An explanation of the term in Eqn. (3.11) is provided: The sub-indices (l,m,n) denote all positive integer numbers and they define the mode. The first term corresponds to the Bessel function, representing the radial distribution. The second term represents the axial distribution. The last term contains the information of both the temporal variation and the circumferential distribution. In this third term $\omega_{l,m,n}$ is the oscillation frequency. Several cases arise from the selection of (l,m,n). However, for simplicity only the first longitudinal and transversal modes are described [9]:

- First longitudinal mode (c.f. Fig. 3.1 lower part): (m=0 and n=0) In these case $j_{0,0} = 0$ and $J_0(0) = 0$. Involving a null radial dependency. This mode cannot be cut-off, so they are not subjected to any restriction and can propagate in the LF range.

- First transversal mode (c.f. Fig. 3.1 upper part): (n = 0, m = 1). According to [9] can be demonstrated than there are not pressure nodes on the radial direction. In addition, the first transversal mode spins in the azimuthal direction (spinning mode). This modes appear in HF oscillations as in the LF range they are cut-off [19]. In section 3.4 the study is limited to this mode, since it is the one exhibiting self-sustained oscillations in the experimental rig [10].

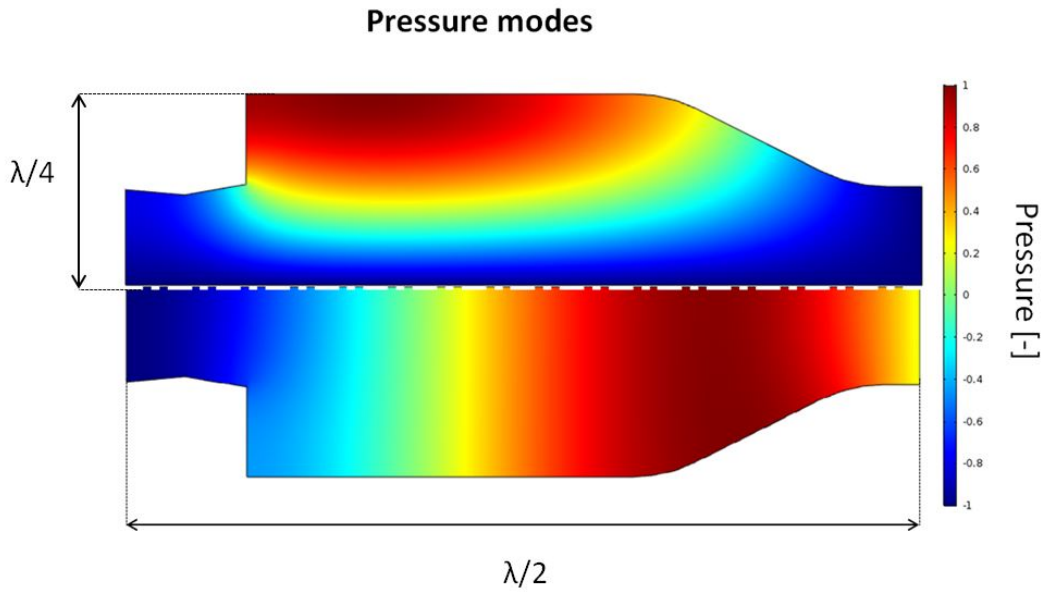

Figure 3.1: Transversal (upper) and longitudinal (lower) first modes

$$\lambda = \frac{c}{f} \tag{3.12}$$

To finish this section, the concept of compactness is discussed. The size of a compact acoustic source is much smaller than the oscillation wavelength, ie. $D << \lambda$. This concept is mathematically defined by means of the Helmholtz number in Eqn. (3.13):

$$He = \frac{l_F}{\lambda} = \frac{l_F\, f}{c} = {}^{1}\begin{cases} << 0.1, & \text{Compact Source} \\ \geq 0.1, & \text{Non-compact Source} \end{cases} \tag{3.13}$$

Using Eqn. (3.12) the frequency and the wavelength can be related. From this relationship HF implies shorter wavelengths and hence the Helmholtz number corresponds to the second case, labelled as non-compact. Fig. 3.1 offers a view of the wavelength for a longitudinal and a transversal mode, which is shorter in the transversal HF mode.

3.3 Flame-Acoustic Interaction in High Frequency Oscillations

In the frame of these thesis, the investigated thermoacoustic oscillations are in the HF range. Therefore, non-compact STFs for the heat release rate fluctuations q' are required that account for the spatial variability of q'. However, according to [22] the fluctuating heat release

[1] Criteria used by the Chair of Thermodynamics in the TUM

rate is one of the least understood phenomena in unsteady combustion problems. Indeed, couplings between the heat release rate fluctuation and the acoustic field were proposed in [22] (e.g. velocity, fuel to air ratio, pressure, temperature and entropy).

Nonetheless, in [11] the unsteady heat release rate q' was coupled with the acoustic velocity and pressure. The capability of this STF to predict the thermoacoustic oscillations was validated in [10] . Therefore, the coupling approach in [11] (Eqn. (3.14)) is employed to explain the heat release rate-acoustic interaction.

$$q'(\mathbf{x},t) = F(\mathbf{u'}(\mathbf{x},t), p'(\mathbf{x},t)) \tag{3.14}$$

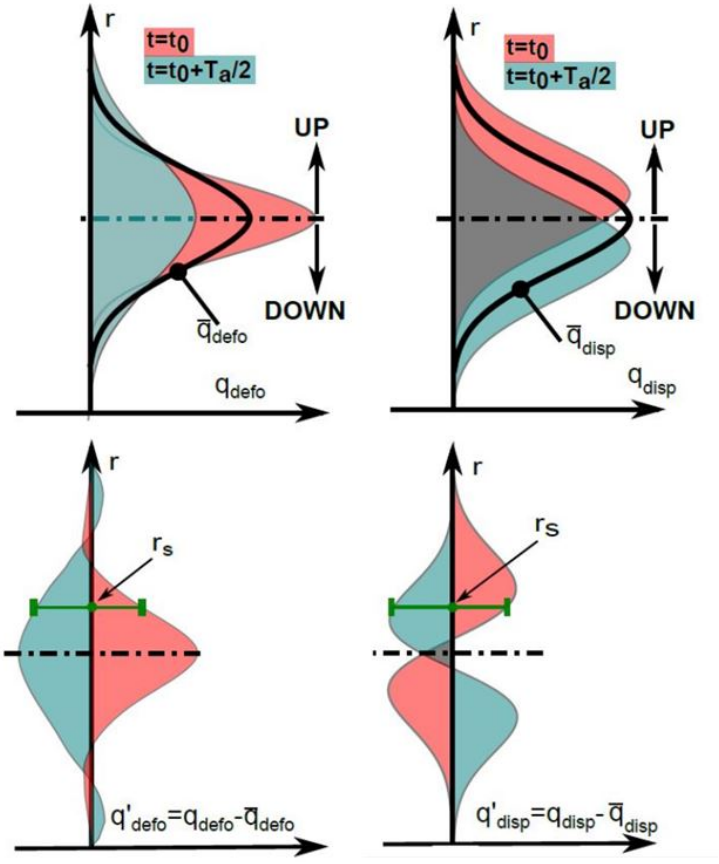

Figure 3.2: Flame deformation (left) and flame displacement (right) [11]

This dependence is described by a STF, also know as Flame Transfer Function (FTF). In the frame of this thesis some mathematical details are skipped, for the complete development see [11]. The flame interaction with acoustic velocity and pressure fields induces a displacement and a deformation in the flame [11]. Fig. 3.2 displays the change in the spatial heat release rate depending on both flame motions. In the top part of Fig. 3.2 the flame position is shown in counter phases of the pressure mode. This flame movement causes a fluctuation

in the spatial heat release rate as seen in the lower part of Fig. 3.2. The objective of the STF is to relate the heat release rate fluctuation to the acoustic field. Eqn. (3.15) uses a first order Taylor expansion to describe mathematically the effects of this motion into the heat release rate:

$$q(\mathbf{x}, t) = \overline{q}(\mathbf{x}) - \nabla\overline{q}(\mathbf{x}) \cdot \Delta'(\mathbf{x}, t) - \overline{q}(\mathbf{x})\nabla \cdot \Delta'(\mathbf{x}, t) \tag{3.15}$$

In Eqn. (3.15) the term $\Delta'(\mathbf{x}, t)$ denotes the acoustic displacement field. It can be expressed in term of acoustic pressure p' and velocity **u'** as it is done in Eqn.(3.16) and Eqn.(3.17) [19].

$$-\nabla \cdot \Delta'(\mathbf{x}, t) = \frac{p'}{\kappa\overline{p}} \tag{3.16}$$

$$\mathbf{u'} = \frac{\partial \Delta'}{\partial t} \tag{3.17}$$

Finally, a linearisation as the one in Eqn. (3.5) is used to relate q with q' (cf. Eqn. 3.18). However, relating $\Delta'(\mathbf{x}, t)$ with the fluctuating velocity is easier in the frequency domain because the Fourier Transform removes the temporal partial derivative in Eqn. (3.17). Next section provides the final STF that is implemented with a FEM.

$$q'(\mathbf{x}, t) = q(\mathbf{x}, t) - \overline{q}(\mathbf{x}) \tag{3.18}$$

3.4 Frequency Domain Formulation

In this section the usage of the Fourier Transform allows transforming the LHE into the frequency domain. The main reason for choosing this formulation is that allows a fast and simple computation in FEM. The calculation in the frequency domain gives explicit access to single eigenfrequencies simplifying the post-processing [11]. The linear and periodic character of the acoustic fluctuations (cf. Sec. 3.1) allows a expansion via a complex Fourier series as it is seen in Eqns. (3.7) and (3.8):

$$\mathbf{u'}(\mathbf{x}, t) = \sum_{n=1}^{N} \hat{\mathbf{u}}_n(\mathbf{x}) exp(-i\omega_n t) \tag{3.19}$$

$$p'(\mathbf{x}, t) = \sum_{n=1}^{N} \hat{p}_n(\mathbf{x}) exp(-i\omega_n t) \tag{3.20}$$

The index n in these expansions denotes the oscillation mode. In the summation the time signal is represented as a superposition of n eigenmodes. Moreover, each mode has a unique spatial distribution at its characteristic oscillating frequency ω_n. An introduction of these discrete variables into equation 3.7 and (3.8) yields the LHE in the frequency domain:

$$i\omega_n \hat{p}_n(\mathbf{x}) + \overline{\rho} c^2 \nabla \hat{\mathbf{u}}_n(\mathbf{x}) = (\kappa - 1)\, \hat{q}_n(\mathbf{x}) \tag{3.21}$$

$$\overline{\rho} i\omega_n \hat{\mathbf{u}}_n(\mathbf{x}) + \nabla \hat{p}_n(\mathbf{x}) = \mathbf{0} \tag{3.22}$$

Next, the partial derivative in Eqn. (3.17) is removed because the Fourier Transform yields Eqn. (3.23):

$$\hat{\Delta}_n(\mathbf{x}) = \frac{\mathbf{u}_n(\mathbf{x})}{-i\omega_n} \tag{3.23}$$

Due to this equation the heat release rate fluctuation can be expressed in the frequency domain in terms of the:

- Mean heat release $\overline{q}(\mathbf{x})$.
- A displacement term with dependency on the velocity $\hat{\mathbf{u}}_n(\mathbf{x})$
- A density term that is a function of the pressure fluctuations $\hat{p}_n(\mathbf{x})$.

Eqn. (3.14) indicated that q' was a function of the acoustic pressure and velocity fields. In Eqn. (3.24) this dependency is separated into a superposition of the acoustic displacement and density. The acoustic velocity is responsible for the displacement and the acoustic pressure for the density.

$$\hat{q}_n(\mathbf{x}) = F(\overline{q}(\mathbf{x}), \hat{\mathbf{u}}_n(x)) + F(\overline{q}(\mathbf{x}), \hat{p}_n(\mathbf{x})) = \nabla \overline{q}(\mathbf{x}) \cdot \frac{\hat{\mathbf{u}}_n(\mathbf{x})}{i\omega_n} + \overline{q}(\mathbf{x}) \frac{\hat{p}_n(\mathbf{x})}{\kappa \overline{p}_n(\mathbf{x})} \tag{3.24}$$

The governing LHE, displayed in Eqns. (3.25) and (3.26), are reduced to the first transversal mode ($n = 1$):

$$i\omega_1 \hat{p}_1(\mathbf{x}) + \overline{\rho} c^2 \nabla \cdot \hat{\mathbf{u}}_1(\mathbf{x}) = (\kappa - 1)\, \hat{q}_1(\mathbf{x}) \tag{3.25}$$

$$\overline{\rho} i\omega_1 \hat{\mathbf{u}}_1(\mathbf{x}) + \nabla \hat{p}_1(\mathbf{x}) = \mathbf{0} \tag{3.26}$$

The model frequency characterises the oscillating thermoacoustic system and predicts its stability. This modal frequency (ω_1) is a complex number as shown in Eqn. (3.27). The real part $\Re[\omega_1]$ is oscillation frequency of the first transversal mode. On the other hand, the imaginary part $\Im[\omega_1]$ describes the temporal change of the acoustic amplitude. If the value is zero the amplitude remains constant. Apart from this case, other two may be observe: Whether $\Im[\omega_1] < 0$ the amplitude decreases, hence the system is damped and stable. Or $\Im[\omega_1] > 0$ the amplitude augments and the system is defined as unstable. In Fig. 3.3 the three different evolutions are plotted.

$$\omega_1 = \Re(\omega_1) + i \cdot \Im(\omega_1) \tag{3.27}$$

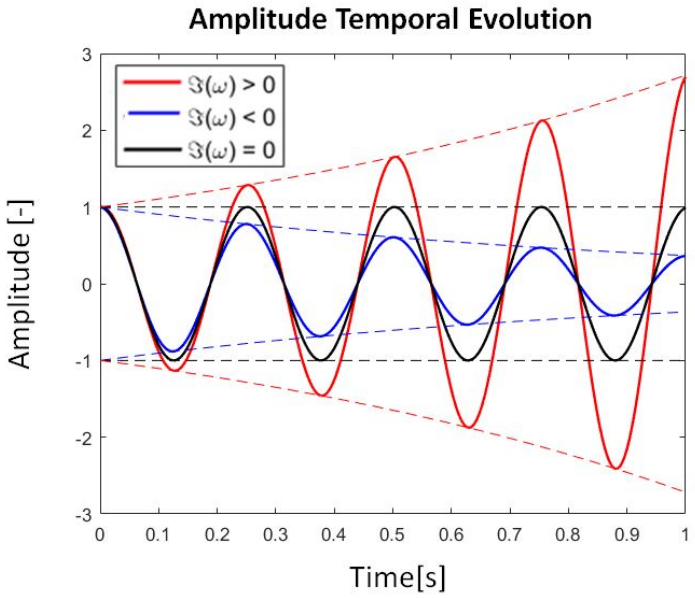

Figure 3.3: Temporal evolution of the three possible oscillation cases

$$\Im(\omega_1) = \nu_1 = \beta_1 - \alpha_1 \tag{3.28}$$

Eqn. 3.28 shows the sign convection proposed by [12]. In the frame of this work no damping processes are considered $\alpha_1 = 0$. Thus $\Im[\omega_1]$ just represents the driving rate $\nu_1 = \beta_1$. This means that in Fig. 3.3 the red line is showing the temporal evolution that is expected to be found in this thesis. From Fig. 3.3 it can be inferred that the final driving rates will have a positive sign (cf. Sec. 5.2).

4 CFD Procedure

This section presents the CFD simulations, which were computed with the commercial CFD software Fluent. The aim of these steady-state simulations is to reproduce the flame in the combustion chamber without any acoustic interaction. The guideline to follow consists of:

- Basic ideas of the flow in the studied combustion chamber.
- The procedure overview.
- An explanation of the isothermal simulation method.
- An explanation of the reactive simulation method.
- An evaluation of the results

4.1 Combustion Chamber Flow Characteristics

In Fig. 4.1 an schematic of the experimental combustor rig is displayed. The premixed and preheated fuel-air mixture comes from a plenum chamber into the A^2EV swirler, which induces a rotational velocity in the mean flow. Thus, in the burner and combustion chamber the flow has a clockwise tangential velocity to stabilize the flame (Chapter 2) [10].

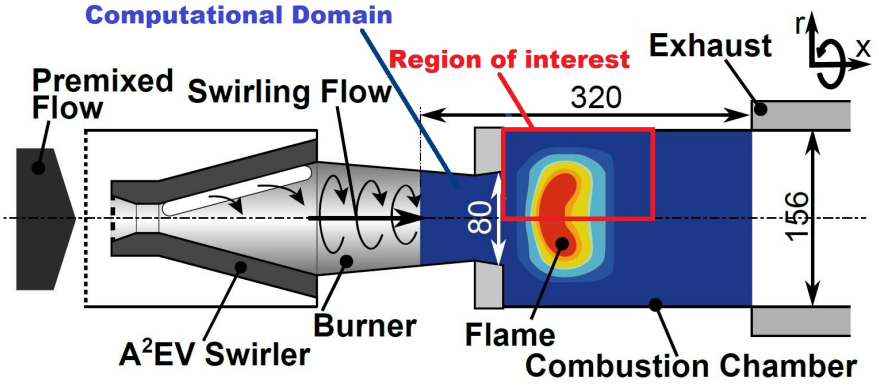

Figure 4.1: Experimental combustor rig [11]

Also, the schematic in Fig. 4.1 includes the computational domain and its dimensions in the blue coloured area for the acoustic-flame interaction performed in Chapter 5. Inside this domain, the region of interest for the reactive CFD simulations is highlighted in red. The effects of this discordance between the computational regions are exposed in Sec. 4.2. Two main flow phenomena occur in the red region:

- The sudden geometry change at the combustion chamber inlet and the fluid viscosity cause a flow detachment.
- The reaction takes place.

The reaction decreases the density in approximately a factor five [17]. Therefore, the flow is compressible. Furthermore, the Reynolds' number is $Re \approx 10^5$ which means that the flow is turbulent [20].

A mean axial velocity distribution, representative of the studied combustor, is presented in the left side of Fig. 4.2. There, two recirculation zones, named inner and outer [22], can be appreciated. They appear because of the flow separation and the later reattachment. In Sec. 4.5 its effect on the temperature field is discussed. The reattachment point is dependent on the swirl intensity due to the circumferential momentum induced by it.

The right part of Fig. 4.2 displays the tangential velocity in the plane A-A. For the studied test rig, the all velocity components are assumed to be axis-symmetric. In the right part of Fig. 4.2 the tangential velocity is shown as an example. This assumption does not match perfectly the real flow in combustor, but it was used in previous works [11].

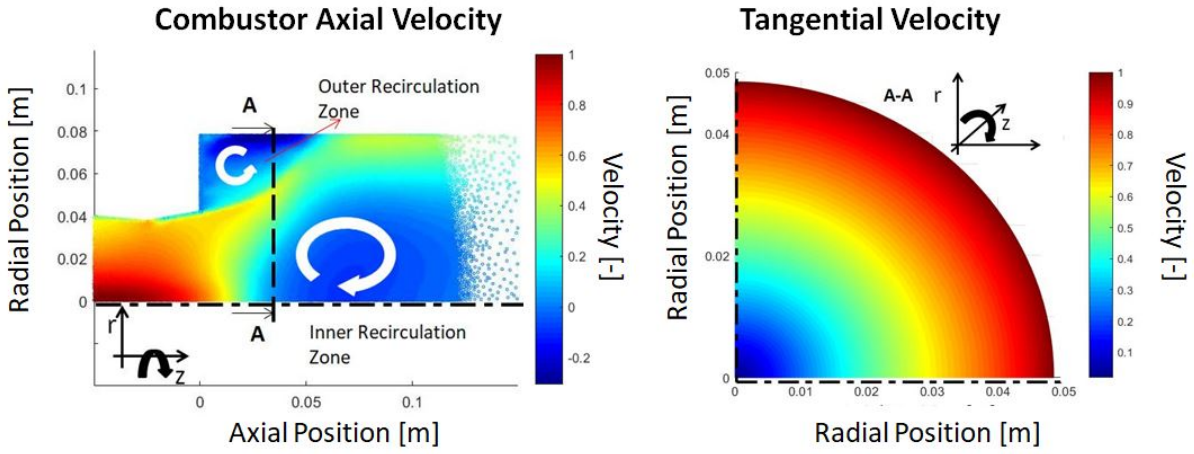

Figure 4.2: Axial velocity in the combustion chamber (left). Tangential velocity in plane A-A (right)

4.2 Procedure Overview

Fig. 4.3 shows the overview of the CFD simulation procedure, which is applied to simulate the lean-premixed combustion in the A2EV configuration shown in Fig. 4.1. The procedure is exemplary shown for the axial velocity component. In the lower half of Fig. 4.3 c), a representative result of a numerically computed heat release rate distribution is displayed. It is based on two CFD simulations: First, the complete test rig velocity and turbulence distribution are obtained by means of an isothermal (no combustion) calculation of just a quarter of the chamber due to the geometry periodicity. Then, a reactive CFD of just 15° of the combustion chamber is performed to simulate the flame behaviour.

From the complete isothermal test rig simulation the profiles at the combustion chamber inlet are extracted (cf. Fig. 4.3 b). Those profiles are assumed to be axis-symmetric as discussed in Sec. 4.1. However, they are not perfectly symmetric after being extracted from the complete test rig simulation. Therefore, the radial values at the 45° angular position are imposed to all the azimuthal positions. Inside the square in Fig. 4.3 b) a white line is shown denoting the 45° angular position of the asymmetric profile and the resulting symmetric profile. These axis-symmetric profiles are used as the inlet boundary condition for the reactive CFD simulations.

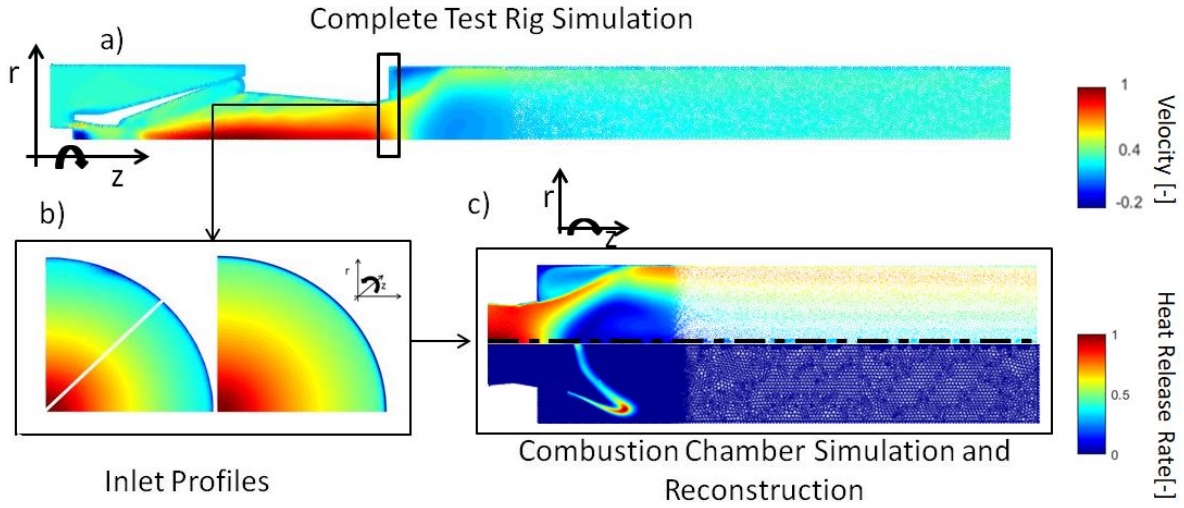

Figure 4.3: Simulation overview

According to [24], the region of interest in CFD should be located at a minimum of five times the inlet radius from the inlet. In this way, the solution is not influenced by the boundary conditions. Consequently, this is a reason enforcing the use of inlet profiles as the boundary condition if only the combustion chamber is desired to be simulated [3].

In Sec. 4.1, it was shown that the computational domain for the acoustic-flame interaction and the CFD region of interest do not exactly match. This means that the burner mean fields,

extracted from the isothermal simulation, must be added to the reactive CFD. The profile displayed in Fig. 4.3 c) is obtained after this reconstruction. The reconstruction is achieved by coupling the isothermal burner profiles with the reactive combustion chamber results through the extracted symmetric inlet profiles. The assumption behind this procedure is that the combustion process exerts negligible effect on the upstream conditions. This assumption was also used in previous works (cf. [14]).

The method requires two CFD simulations and an intermediate processing step to prepare the inlet profiles, but delivers the following advantages:

- Smaller reactive flow simulation size enabling a higher flame resolution without a computational cost increase.
- Capability of maintaining the axis-symmetry assumption.

4.3 Isothermal Simulation

This section aims to explain the computational domain and mesh for the isothermal case. Besides that, the models and the boundary conditions that allow the reproduction of the test rig are described.

4.3.1 Computational Domain, Mesh and Models

Fig. 4.4 presents the complete test rig computational domain. This numerical domain represents the the spatial dimension of the test rig. However, the combustion chamber length differs from the real one, the CFD geometry is 230 mm longer. The reason for that is to avoid that the outlet boundary affects our solution [24].The simulation domain also takes only a quarter of the complete chamber.

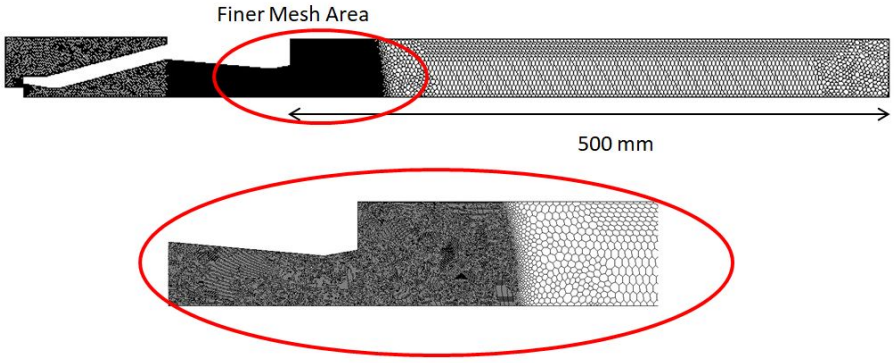

Figure 4.4: Isothermal CFD computational domain and mesh

The mesh is also included in Fig. 4.4 along with a detail of it. The mesh is characterised by unstructured cells with a polyhedral shape. The polyhedral mesh has the advantage of requiring less elements than a tetrahedral mesh and shows a higher element quality [3]. Furthermore, the consistency of the results is better than other implemented meshes (ie. structured). The hypothesis to explain this behaviour is that in a structured mesh the swirled flow never encounters the cells in a 90º angle. The possibilities of a 90º flow-cell encounter are enhanced in a polyhedral mesh. The implemented mesh shows a refined region at the combustion chamber inlet since the velocity and turbulent profiles for the reactive simulation are extracted at that position (Sec. 4.3). Tab. 4.1 includes the statistical data of this mesh.

Table 4.1: Isothermal mesh statistics

Case	Type of mesh	Number of elements	Element density $\left[\frac{Elements}{cm^3}\right]$
Isothermal	Unstructured polyhedra	12207286	2396.3

In Sec. 4.1, the flow separation was mentioned as one of physical phenomena responsible for modelling the combustion. According to [14], the $k-\epsilon$ turbulence model is able to capture the flow detachment in the studied combustor layout. In [2] the information about this model is found. It is a two equation model that solves the turbulent kinetic energy (k) and the dissipation rate (ϵ). The most important aspects are:

- Suitability for rotating flows, ie. swirl-established flows.
- Boundary layer separation can be good described by this model.
- Ability to predict sudden changes in strain.
- Flexibility in the wall resolution. The model can either use a standard wall function or adapt the wall function for fine meshes.

4.3.2 Boundary Conditions

Table 4.2: Isothermal boundary conditions for each operational point

Operational Point	Temperature [K]	Mass Flow $[g/s]$	Outlet	Walls
OP 1	623.15	80	Outflow	No Slip
OP 2	623.15	80	Outflow	No Slip
OP 3	623.15	120	Outflow	No Slip
OP 4	623.15	120	Outflow	No Slip

Tab. 4.2 gathers the operational point boundary conditions for the isothermal case. The inlet requires a temperature information, which is the plenum temperature, to calculate the fluid density [2]. The mass flow entering the test rig from the plenum is also necessary. Additionally, the turbulence boundary conditions must be given at the inlet [3]. In the isothermal case the proposed values by [2] for the turbulent intensity and the viscosity ratio are taken. Indeed, simulations varying this parameters were implemented and its impact on the results was negligible.

The outlet behaviour is captured using an outflow without affecting the flow behaviour. The outflow boundary condition sets the flow gradients to zero [3].

The walls are impermeable, rigid, adiabatic and static. This implies that there is no exchange of mass or heat. Therefore, the only condition that must be fulfilled is the no slip one. The no slip condition can be schematically seen in Fig. 4.5, it is based on the assumption that the relative velocity between a particle located next to the wall and the wall itself is zero.

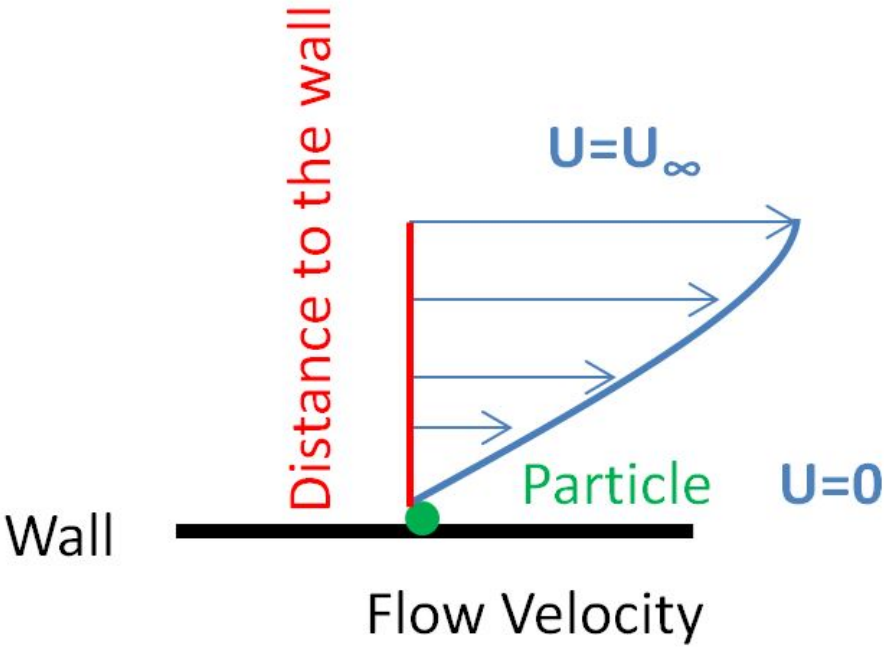

Figure 4.5: Diagram showing the no slip condition

Owning to the periodicity of the A^2EV combustor configuration, the simulation accounts only for a quarter of the chamber. For this reason a periodic boundary condition is imposed in the symmetry planes [3].

4.4 Reactive Simulation

The objective of this section seeks to present the reactive case as in Sec. 4.3 does with the isothermal CFD.

4.4.1 Computational Domain and Mesh

In this simulation the computational domain is restricted to the combustion chamber, which has the same length as the isothermal case, as can be displayed in Fig. 4.6. The axis-symmetric inlet profiles allow a 15º simulation. This reduces the simulation volume, which has a positive impact on the computational cost and the achievable mesh resolution.

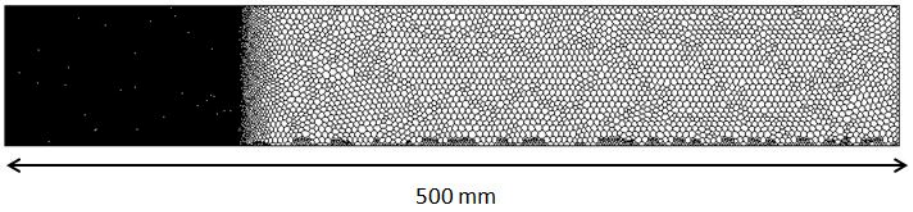

Figure 4.6: Computational domain and mesh for the reactive case

The mesh shares most of the characteristics of the isothermal case. This involves a polyhedral unstructured mesh with a refinement in the combustion area. Even though the number of cells is smaller than in the isothermal case, the amount of elements per volume is about three times higher (cf. Tab. 4.3). This allows a highly resolved flame and mean flow profiles in the area of interest.

Table 4.3: Reactive mesh statistics

Case	Type of mesh	Number of elements	Element density $\left[\frac{Elements}{cm^3}\right]$
Isothermal	Unstructured polyhedra	5388696	6766.4

The convergence criteria for this thesis is based on the turbulent kinetic energy. The calculation is considered to be converged if the volume-averaged turbulent kinetic energy remains constant with respect to increasing number of iteration steps [3]. The upper part of Fig. 4.7 shows a representative trend of the volume-average turbulent kinetic energy of the reactive simulation. Convergence can be assumed after about 6000 iterations.

To assess the mesh independence an analysis is conducted as proposed by [15]. This analysis is also based on the turbulent kinetic energy, if it is constant regardless of the number of elements, the mesh can be considered as independent. In the lower part of Fig. 4.7 it can be appreciated that the volume-averaged turbulent kinetic energy is almost constant from 2671378 elements onwards. Therefore, the simulation is both converged and mesh independent.

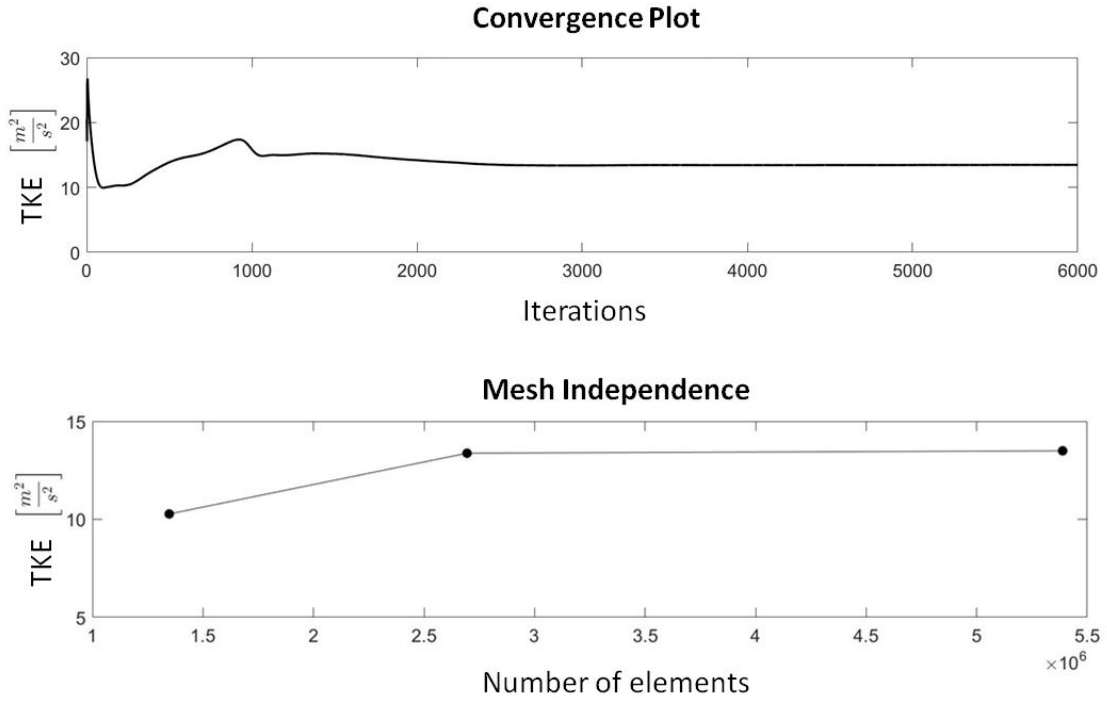

Figure 4.7: Convergence and mesh independence plots

4.4.2 Flame Model

Combustion is a chemical process in which the reactants are transform into products releasing thermal energy. These process involves a large number of species. Therefore, the computational cost of solving a transport equation for each specie makes this approach infeasible. Due to this reason, in reactive CFD flows a correct selection of a flame model is critical to obtain a representation matching the real flame with an acceptable computational cost. Hence, the first step to find the most suitable model is summing up the flow properties for the studied combustor in Sec. 4.1. Those key characteristics are:

- Premixed Species
- Turbulent-Swirled Flow

- Lean Combustion

This means, there is a chemical process taking place in a turbulent flow, so the turbulent-chemistry interaction has to be assessed. To do so, the Karlovitz number is introduced in Eqn. (4.1) This dimensionless number relates the chemical time scale with the smallest turbulent time scale, also known as Kolmogorov time scale [14]. Turbulent and chemical time scales can be rewritten in terms of flame thickness (δ_F) and Kolmogorov scale (η).

$$Ka_t = \frac{t_F}{t_\eta} = \frac{\delta_F^2}{\eta^2} \tag{4.1}$$

The Karlovitz number help to distinguish between flames suffering from different levels of turbulent-chemistry interaction. The visualisation of this regions is easier using the Borghi's diagram included in Fig. (4.8). Borghi's diagram makes dimensionless the flame length in the x-axis using the ratio between turbulent and laminar lengths $\frac{l_{turbulent}}{l_{laminar}}$. Also this turbulent to laminar ratio is used to make dimensionless the flame speed in the y-axis. Three different zones can be appreciated but only two of them are found in gas turbine combustors [17] and [14]:

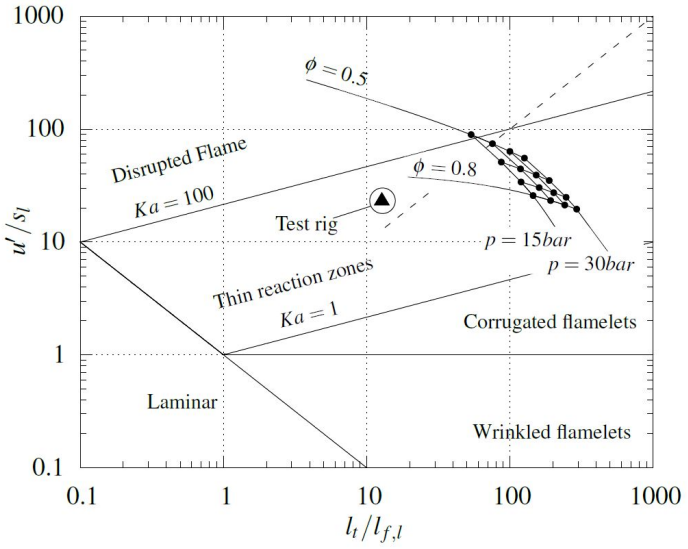

Figure 4.8: Borghi's diagram [14]

- Thin reaction zone: The region between, the lines of $Ka_t = 1$ and $Ka_t = 100$. The smallest turbulent structures are bigger than the reaction layer. Therefore, the combustion retains its one dimensional character. Both gas turbines and the test rig in Sec. 4.1 work in the thin reaction zone (cf. 4.8)

- Disrupted Flame: Characterised by $Ka_t > 100$ which involves a strong turbulence influence in the chemical processes. Hence a 1D flame front assumption is no longer held.

According to [21] and [14], gas turbines operate in the zone of thin reaction, which means that a 1D flamelet simplification is valid. The term flamelet is used in CFD terminology to refer to premixed flame fronts [17]. From Borghi's Diagram the combustion models based on the assumption that turbulent scales are much larger than chemical can be discarded since they involved $Ka_t > 100$.

The validity of 1D flamelets for gas turbines lead to consider the Flame Generated Manifold (FGM) model as a suitable flame model for the combustor configuration in this thesis. This model validity for gas turbine combustors was shown by [14]. Its approach consists of gathering the thermo-chemical state into two transported variables (Eqns. (4.2) and (4.3)) [21]. In this case the transported variables are [2]:

- The progress variable (c) it is bounded between 0 and 1. It indicates the amount of formed products in a spatial position.
- The mixture fraction (f), standing for the amount of oxidizer in the premixed working fluid.

$$\overline{\rho}\frac{\partial c}{\partial t} + \overline{\rho}\frac{\partial}{\partial \mathbf{x}}(\mathbf{u}\, c) = \overline{\rho}\frac{\partial}{\partial \mathbf{x}}\left(\frac{\nu_t}{Sc_t}\frac{\partial c}{\partial \mathbf{x}}\right) + \overline{\dot{\omega}_c} \tag{4.2}$$

$$\overline{\rho}\frac{\partial f}{\partial t} + \overline{\rho}\frac{\partial}{\partial \mathbf{x}}\left(\mathbf{u}\, f\right) = \overline{\rho}\frac{\partial}{\partial \mathbf{x}}\left(\frac{\nu_t}{Sc_t}\frac{\partial f}{\partial \mathbf{x}}\right) \tag{4.3}$$

This representation allows to use the c-space (1 dimensional) instead of the spatial coordinates (3 dimensional) (cf. Eqns. (4.4) and (4.5)) [2]. The c-space consist of expressing the reaction variables (temperature and species) as a function of the progress variable (c). The approach reduces the number of equations to solve because each specie is described with one equation (c-space) instead of three (spatial coordinates), reducing the computational cost [2].

$$\overline{\rho}\frac{\partial T}{\partial t} + \frac{\partial T}{\partial c}\dot{\omega}_c = \overline{\rho}\chi_c\frac{\partial^2 T}{\partial c^2} - \frac{1}{c_p}\sum_k h_k\dot{\omega}_k + \frac{\overline{\rho}\chi_c}{c_p}\left(\frac{\partial c_p}{\partial c} + \sum_k c_{p,k}\frac{\partial Y_k}{\partial c}\right)\frac{\partial T}{\partial c} \tag{4.4}$$

$$\overline{\rho}\frac{\partial Y_k}{\partial t} + \frac{\partial Y_k}{\partial c}\dot{\omega}_c = \overline{\rho}\chi_c\frac{\partial^2 Y_k}{\partial c^2} + \dot{\omega}_k \tag{4.5}$$

In Eqns. (4.4 and 4.5) the term Y_k stands for the k_{th} species, ω_k denotes the mass reaction rate corresponding to the k_{th} species. The scalar dissipation rate (χ_c) escalates the temperature diffusion in the c-space $\left(\frac{\partial^2 T}{\partial c^2}\right)$. The way this term is modelled can be found in [2] and in [3] values for this parameter are recommended.

The reaction term ($\overline{\dot{\omega}_c}$) must be closed because the system has one more unknowns than equations. It can be seen in Eqn. (4.2) that this term is not only necessary to close the temperature and species evolution in c-space but also the spatial transport of c. To do so, the 1D flamelet simplification is used. Therefore, the reaction term value ($\overline{\dot{\omega}_c}$) is tabulated as a function of c and f. In this process the effect of turbulence-chemistry is accounted by the use of Probability Density Functions (P), given in Eqn. (4.6). The determination of PDFs in this problem was done by means of the external software Cantera [14]. However, the calculation of the reaction term ($\overline{\dot{\omega}_c}$) represents the main model weakness since non-adiabatic effects and flame stretch are not consider. Hence, overestimations of the reaction term occur in the regions of high heat loss or high stretch.

$$\overline{\dot{\omega}_c^0} = \int\int \dot{\omega}_c^0(c,f) \cdot P(c) \cdot P(f) \cdot dc \cdot df \tag{4.6}$$

In order to improve the results in these regions without adding computational cost to the method a correction term is proposed by [14], transforming Eqn.(4.6) into Eqn.(4.7).The correction term escalates ($\overline{\dot{\omega}_c^0}$) to avoid overestimations of the reaction rate. This correction term ($\Gamma(\kappa,\psi,f)$) measures the ratio between the stretched, diabatic flame speed ($s_c^*(\kappa,\psi,f)$) and the unstretched, adiabatic speed ($s_c^0(f)$). The ratio is not applied linearly but powered to a constant (m) as shown in Eqn. (4.8).

In [21] the possible values of the constant m for Eqn.(4.8) are discussed. Its value is in the magnitude order of unity. Also in [21] the calculation method for the stretch (κ) and heat loss (ψ) is explained.

$$\overline{\dot{\omega}_c^*} = \Gamma(\kappa,\psi,f) \int\int \dot{\omega}_c^0(c,f) \cdot P(c) \cdot P(f) \cdot dc \cdot df \tag{4.7}$$

$$\Gamma(\kappa,\psi,f) = \left(\frac{s_c^*(\kappa,\psi,f)}{s_c^0(f)}\right)^m \tag{4.8}$$

Summing up, the FGM Extended model used in the frame of this thesis allows a flame speed reduction or disappearance in high stretched and strongly diabatic regions without the use of extra transport equations. Therefore, the flame front is thickened and the shear layer burning is avoided or improved with respect to the standard FGM. Fig. 4.9 displays a comparison between both. It can be noticed that the shear layer burns weaker in the extended case and the reaction position is also better predicted.

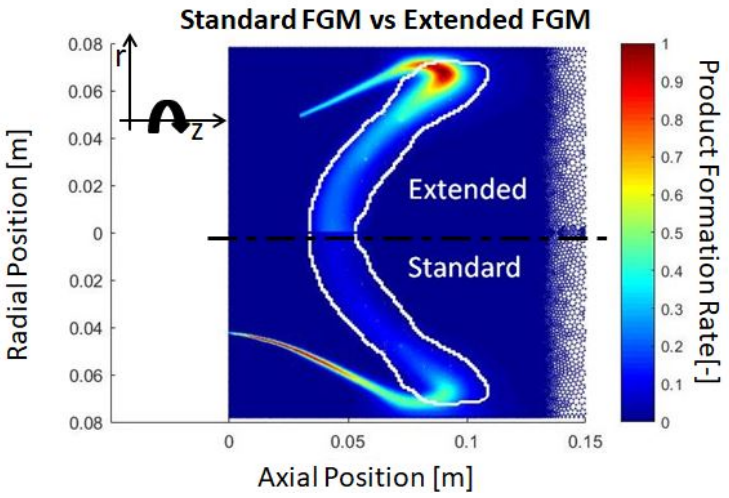

Figure 4.9: Comparison between the standard and the extended FGM models

The turbulent model recommended to use with this flame model by [14] is the $k-\epsilon$. This model is the same one implemented in the isothermal case in Sec. 4.3.1.

4.4.3 Boundary Conditions

Tab. 4.4 collects the inlet boundary conditions of all the operational points. The inlet mass flow is not directly imposed but it appears implicitly in the inlet symmetric profiles extracted from the isothermal simulation. These profiles comprise of the velocity components: Axial, tangential and radial. Alongside with the turbulence components: Turbulent kinetic energy and dissipation rate.

Table 4.4: Boundary conditions for each operational point

Operational Point	Temperature [K]	Mass Flow $[g/s]$	Mixture Fraction [-]	λ [-]
OP 1	623.15	80	0.03136	1.8
OP 2	623.15	80	0.04626	1.2
OP 3	623.15	120	0.03136	1.8
OP 4	623.15	120	0.04626	1.2

The inlet temperature is the preheated one at the plenum and the mean mixture fraction can be calculated by means of Eqn. (4.9):

$$f = \frac{\dot{m}_{fuel}}{\dot{m}_{fuel} + \dot{m}_{air}} \tag{4.9}$$

The outlet boundary condition is identical as in Sec. 4.3.2 for the isothermal case: An outflow boundary condition.

The walls show a difference with the isothermal CFD. In the reactive case heat losses through the walls are considered. Those are not neglected in this case due to combustion high temperature. The approach is based on the Newton's law of cooling in Eqn. (4.10) [20]. The heat transfer per unit area in Eqn. (4.10) is proportional to the temperature difference. The proportionality coefficient (h) is available in the literature and an recommended value for a free convection problem is $h = 150 \left[\frac{W}{m^2 K}\right]$ [20].

$$\frac{\dot{q}}{A} = h \cdot \Delta T \tag{4.10}$$

On the other hand, the walls share the non-slip conditions with the isothermal case in Sec. 4.3.2. Another common boundary condition for both cases is the periodic boundary at the interface. However, in this case the periodicity occurs each 15º instead of every 90º, due to the amount of simulated chamber.

4.5 Results

In this section, the results of CFD simulations are presented. First, a brief qualitative explanation about the experimental data used for the comparison is given. Afterwards a comparison between the experimental and CFD simulation images is performed for the temperature distributions. The product formation rate obtained from CFD simulations is compared against the OH* distribution from experiments. Among the four calculated points just two of them are discussed (OP 2 and OP 3) because they have different mass flows and fuel-to-air ratios. Then the velocity profile is reviewed.

The approach to obtain the experimental OH* distribution is explained in [10]. The procedure in [10] is based on the OH* chemiluminescence phenomena, involving that the formation of OH radicals emits light. Therefore, the flame can be recorded and then the OH* distribution is averaged during a complete oscillation cycle to obtain the heat release rate for a cut-plane applying the inverse Abel transform [10]. The temperature field, which is obtained via a single, representaive reactive CFD simulation [14],is fitted to the experimentally recorded OH* distributions [10].

The key limitation of this method is that disturbances are also averaged (e.g. fluctuations on the mixture fraction, mass flow oscillations, etc.) cause a continuous flame displacement which is recorded. Thus, the flame thickness is bigger than the instantaneous flame thickness. Another limitation is the flame being affected by the acoustic interaction. It results in heat release rate differences with respect to a combustion process without thermoacoustic effects. For further details see [10].

The first operational point to be analysed is the OP 3, which exhibits an air mass flow of 120 $\frac{g}{s}$ and $\lambda = 1.8$. The upper part of Fig. 4.10 shows the heat release rate comparison. The qualitative flame shape in both cases fits reasonably. However, the CFD simulated flame still shows a small burning in the shear layer region. Additionally, the maximum heat release rate location of both pictures does not match. The experimental data has the maximum heat release rate located in a central position while the CFD displays a maximum towards the walls. The motives for this difference are later explained (cf. Fig 4.11).

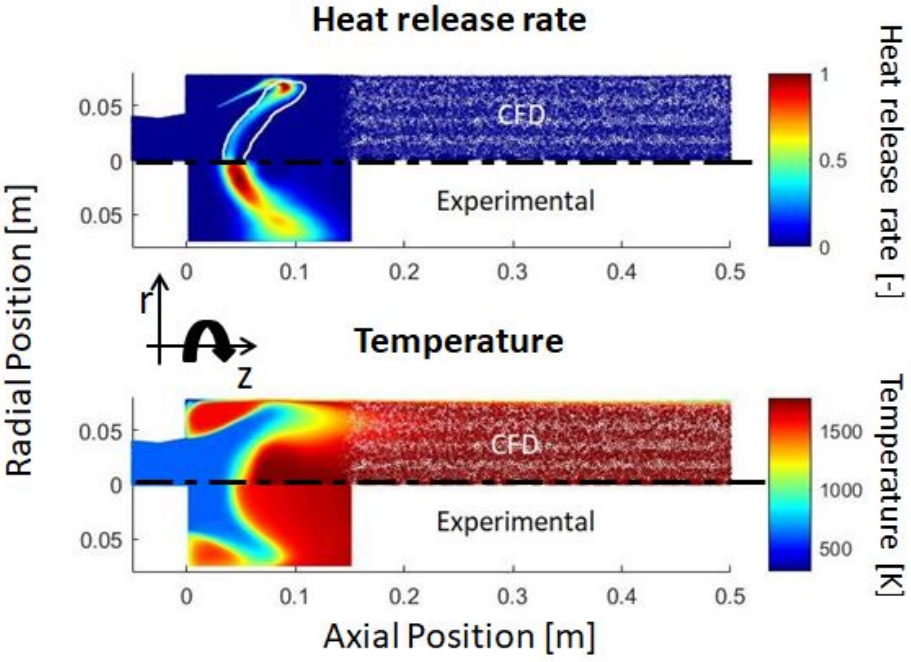

Figure 4.10: Heat release rate distribution (upper) and temperature field (Lower) comparison. OP 3

The second field to be compared is the temperature field in the lower part of Fig. 4.10. The temperature change is coupled to the heat release rate, whose axial position in the numerical case fitted the experimental image. Thus, the axial temperature distribution is almost identical. Both recirculation zones present the same temperature increase. However, Downstream the flame and outside the inner recirculation zone the biggest temperature deviation occurs. That region shows a lower temperature in the CFD simulations than the estimated experimental temperature.

Now, the other operational point (OP 2) is assessed. In this case, the mass flow is 80 $\frac{g}{s}$ and the mixture is richer with a $\lambda = 1.2$. The most important difference is that OP 2 is a thermoacoustically unstable operational point [10]. In concrete, the instability is governed by the first transversal mode of the combustion chamber. This involves significant higher oscillation amplitudes than stable configurations. As it was explained in Chapter 3 instabilities

in the HF range usually excite transversal modes. Due to absence of acoustics in the steady-state simulations, the instability is not captured in this images.

Fig. 4.11 illustrates the difference between an exemplary point working in stable and unstable conditions. An implemented Helmholtz Resonator suppresses any the thermoacoustic instability yielding the left distribution where maximum heat release rate is located closer to the walls. The unstable counterpart is shown on the right. Due to the unstable character a displacement of the mean heat release rate towards the symmetry axis can be observed. According to [13], an acoustically affected flame keeps the driving rates constant. Hence, the CFD heat release rate and temperature field difference, in unstable points, with respect to the experimental images should not affect the final driving rate [13].

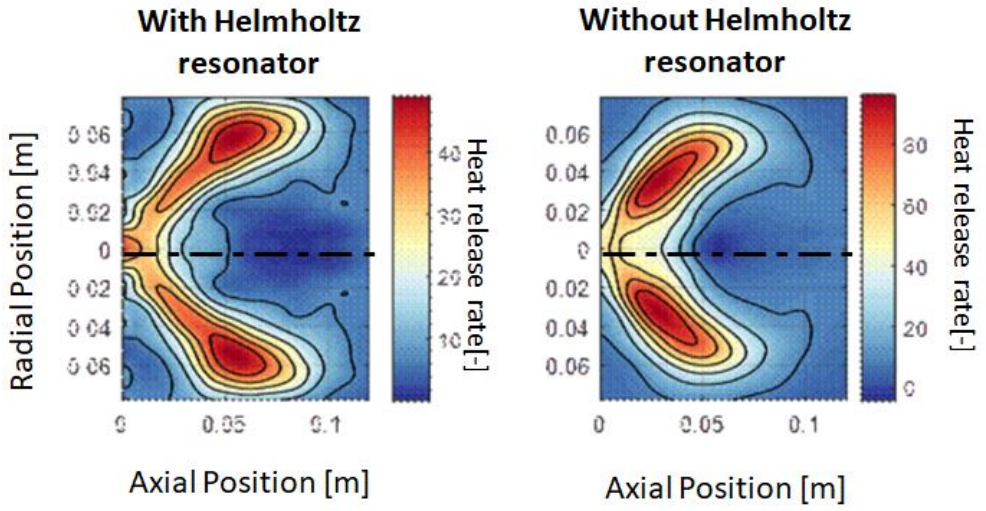

Figure 4.11: Heat release rate with Helmholtz Resonator (left) and without (right) [13]

In Fig. 4.12 both OP 2 CFD temperature and heat release rate fields are plotted in comparison to the experimental data. The upper part, shows again the heat release rate. Both axial flame positions are located at around 50 mm from the chamber inlet. The phenomena described in Fig. 4.11 can be also observed in Fig. 4.12: The heat release rate maximum of the experimental image is located more centred than the CFD simulated heat release rate maximum.

In the lower part of Fig. 4.12 the temperature fields are compared. Even though in this case the difference in this field is bigger than in the previous one, the trends are the same:

- The axial flame position fits.
- The temperature inside the recirculation zones is homogeneous and matches the experimental data. However, the CFD simulation of OP 2 displays a lower temperature in the outer recirculation zone than in the experimental images.
- The region downstream of the flame and outside the recirculation zones shows in both cases the biggest deviation between CFD and experiments.

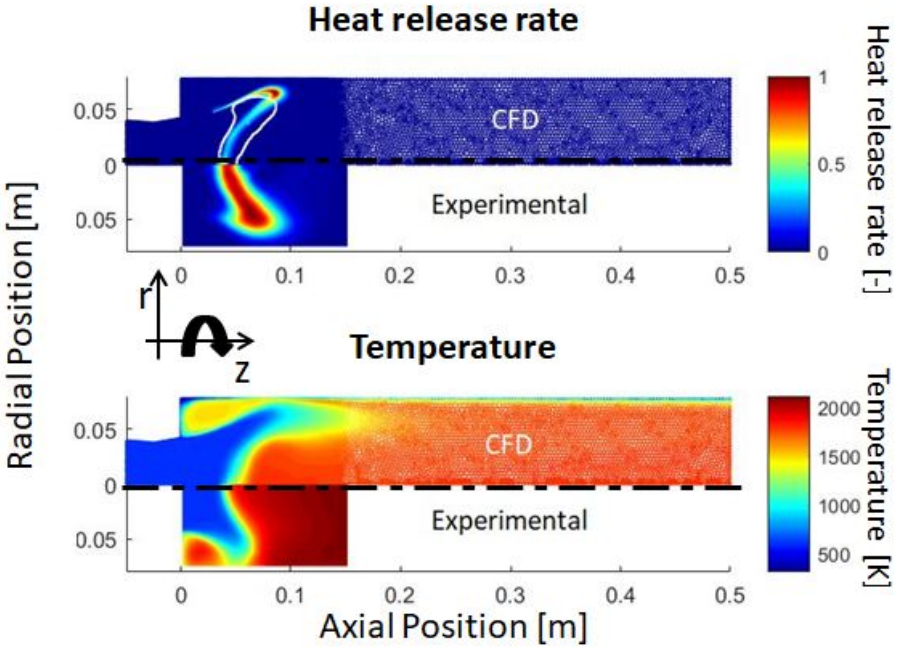

Figure 4.12: Heat release rate distribution (top) and temperature field (bottom) comparison. OP 2

It is important to mention that the deviation in the temperature profile causes difference in the oscillation frequency. Due to the lower temperature in the outer recirculation zone, the oscillation frequencies of the CFD obtained data are expected to be smaller . This concept is explained in chapter 5. To finish this comparison, a small summary of the ideas exposed is provided in Tab. 4.5.

Table 4.5: Table gathering the comparison similarities and differences

Case	Field	Similarities	Differences
OP 12.1	Formation Rate	Axial Position	Location of the Maximum
		Flame Shape	
	Temperature	Axial Position	Smaller Growth Gradient
		Inner and Outer Recirculation	
OP 10.4	Formation Rate	Axial Position	Location of the Maximum
	Temperature	Axial Position	Smaller Growth Gradient
		Same Trend	Smaller Global Temperature

Finally, the velocity profiles are discussed. All the operational points show the same trend. Therefore, the point OP 4 is the only one shown here. The velocity profiles are of minor interest in the frame of this thesis because the FEM just requires the mean temperature and heat release rate fields. However, it is interesting to check if the axial velocity profile fulfils

the forecast trend in Sec. 4.1. Fig. 4.13 aims to prove that the CFD simulation predict the recirculation areas. Hence, both recirculation zones are marked and it can be appreciated that effectively a backflow occurs. Another remark is that the region of maximum velocity coincide with the region of bigger temperature deviation between CFD and experiments. Thus, a possible hypothesis to explain this temperature deviation is: CFD takes into account the velocity to calculate the temperature. Whereas the experimental data may be using escalating factors to estimate the temperature that neglect this phenomena.

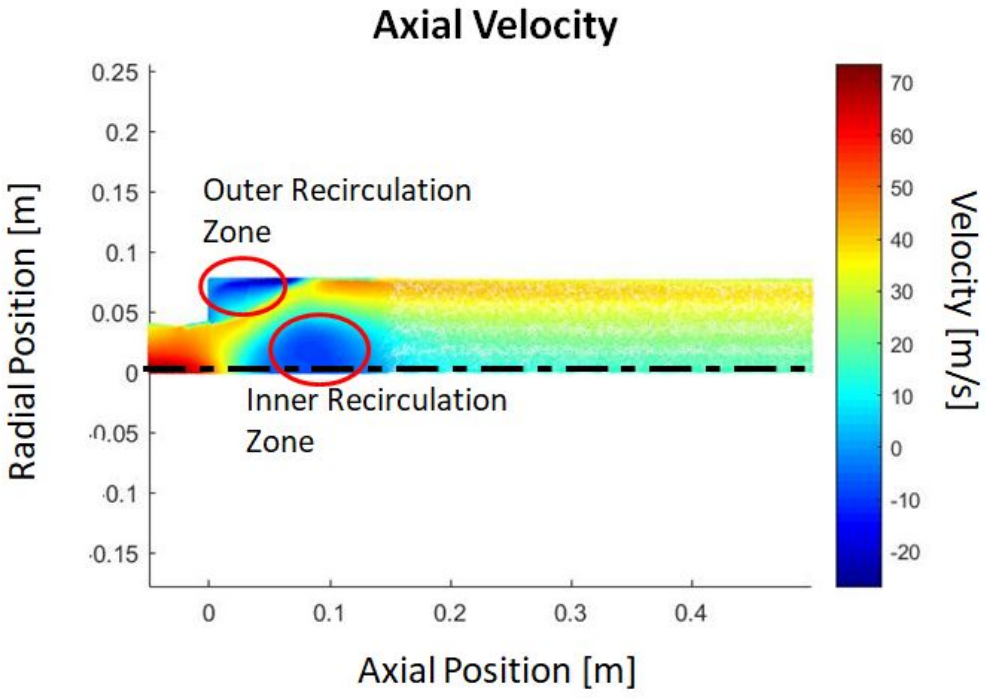

Figure 4.13: Axial velocity profile for OP 4

5 FEM Procedure

The objective of this chapter is to compute the modal frequency ω_1 in Eqns. (5.1) and (5.2) introduced in Chapter 3. The implementation of a FEM to solve the eigenfrequency problem in Eqns. (5.1) and (5.2) employs the commercial software COMSOL. The inputs for these equations (i.e. mean heat release rate and mean temperature field) are obtained in Chapter 4 using steady-state CFD simulations.

$$i\omega_1 \hat{p}_1(\mathbf{x}) + \overline{\rho} c^2 \nabla \cdot \hat{\mathbf{u}}_1(\mathbf{x}) = (\kappa - 1)\, \hat{q}_1(\mathbf{x}) \tag{5.1}$$

$$\overline{\rho} i\omega_1 \hat{\mathbf{u}}_1(\mathbf{x}) + \nabla \hat{p}_1(\mathbf{x}) = \mathbf{0} \tag{5.2}$$

The mean heat release rate calculation requires a brief explanation. From the CFD simulations in chapter 4 the product formation rate indicates the formation rate $\overline{\dot{\omega}_c}$ [2], which was introduced in section 4.4.2. However, the CFD does not directly provide the local mean heat release rate. The following assumptions are done:

- The chemical reaction is considered to be completed in the flame region. This involves that the total heat release rate Q_{th} can be calculated in Eqn. (5.3). The calculation requires the fuel mass flow $\dot{m}_F$ and the heat of combustion or lower heating value of the fuel H_i.
- The local mean heat release rate $\bar{q}(\mathbf{x})$ depends only on the formation rate $\overline{\dot{\omega}_c}$. Additionally, the relationship between the formation rate $\overline{\dot{\omega}_c}$ and the local mean heat release rate $\bar{q}(\mathbf{x})$ can be assumed as linear (cf. Eqn. (5.4)) [10]. Therefore, the determination of a scaling factor is the only requirement to calculate the local mean heat release rate $\bar{q}(\mathbf{x})$.

$$Q_{th} = \dot{m}_F \cdot H_i \tag{5.3}$$

$$\bar{q}(\mathbf{x}) = K\, I(\mathbf{x}) \tag{5.4}$$

The calculation of the scaling factor K is shown in Eqn. (5.5). It is based on computing the ratio between the total heat liberated in the combustion chamber Q_{th} and the total formation of species $\int_V I(\mathbf{x}) \cdot dV$.

$$K = \frac{Q_{th}}{\int_V I(\mathbf{x}) \cdot dV} \tag{5.5}$$

5.1 Computational Domain and Boundary Conditions

In this section the specified FEM computational domain, mesh and boundary conditions are presented. The usage of the 2D Bloch [1] permits approaching the problem as a two-dimensional, even though it is a 3D.

In the top part of Fig. 5.1 the first transversal mode pressure distribution and its boundary conditions are displayed. The pressure transversal modes is cut-off approximately at the middle of the combustion chamber. The physical reason is the increase of temperature towards the outlet. The associated speed of sound increase provokes the augment of the cut-off frequency [19]. Therefore, this transversal mode cannot propagate further downstream.

$$Z = \frac{p'}{u'} \tag{5.6}$$

The inlet and outlet boundary conditions are defined by the acoustic impedance (cf. Eqn. 5.6). In the inlet the geometry change causes a total wave reflection. Therefore, the inlet is considered as a rigid wall whose axial acoustic velocity is zero $u'_x = 0$, resulting into $Z = \text{inf}$. The outlet is defined as an open boundary with a null acoustic pressure $p' = 0$, which entails a zero acoustic impedance $Z = 0$. However, the evanescence of the transversal mode also induces a zero fluctuating velocity $u' = 0$. It yields the disappearance of the acoustic intensity flux (cf. Eqn. 5.7) at the outlet. This means that the outlet is energetically neutral so that the outlet boundary condition does not affect the results [11].

$$\mathbf{I}(\mathbf{x}, t) = p' \, u' \tag{5.7}$$

The acoustic velocity normal to the walls vanishes $\mathbf{u'} \cdot \mathbf{n} = 0$. The final boundary condition in the symmetry plane does not constrain neither the acoustic pressure nor the velocity.

[1] Provided by my supervisor.

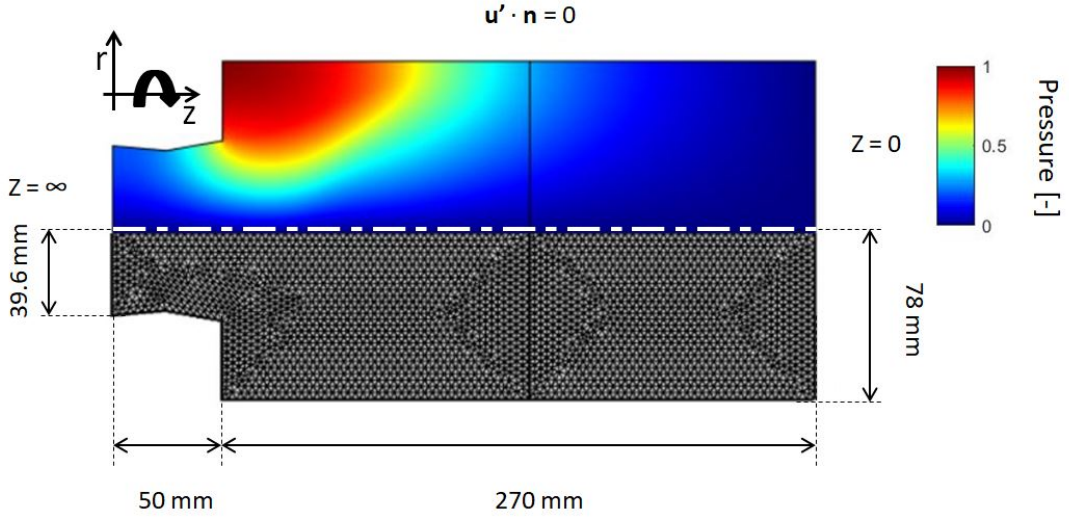

Figure 5.1: First transversal mode with the specified boundary conditions (top). FEM computational domain and mesh (bottom)

The bottom part of Fig. 5.1 shows the computational domain. The combustion chamber computational domain for the FEM simulation matches the dimensions in Fig. 4.1, which was not possible in the CFD simulation (cf. Chapter 4). This is feasible due to the energetically neutral outlet. Moreover, Fig. 5.1 presents the case mesh, which statistical data is gathered in Tab. 5.1.

Table 5.1: FEM mesh statistics

Type	Non-structured triangular
Number of elements	4901
Minimum element quality	0.875

5.2 Results

This section aims to present the final driving rates results. The objective of the linear stability analysis is to validate the developed method's capability to predict thermoacoustic instabilities. The validation is based on comparing the experimentally with the numerically obtained results. First, the transversal pressure modes are compared. The exemplary operational points are the same as in Sec. 4.5. Then, the Rayleigh's indices for OP 1 are discussed. Finally, a quantitative comparison of all the driving rates and both contributions (displacement and deformation) is presented.

The first point to compare is OP 3. In Fig. 5.2 the pressure fluctuations of the first transversal mode can be seen. From a first qualitative comparison both images exhibit a similar pressure mode shape. However, the CFD simulation shows a longer pressure mode: This is linked with the temperature comparison done in section 4.5. In the CFD simulations the temperature maximum is located further downstream than in the experimental estimations. Therefore, the modal frequency is smaller. Additionally, the lower temperature in the outer recirculation zone in comparison to the experimental images provokes a lower cut-off frequency.

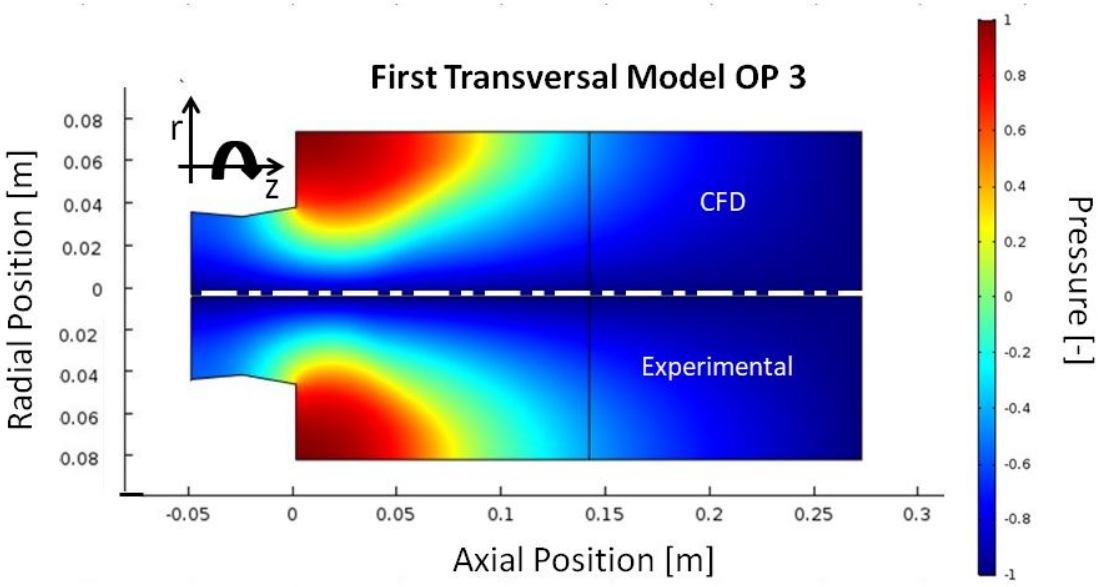

Figure 5.2: Amplitude distribution of fluctuating pressure at the first transversal eigenmode for the reactive case OP 3.

Fig. 5.3 shows the pressure mode of the OP 2. Again the same trends can be observed: On the one hand, the CFD simulation fits with an acceptable accuracy to the experimental data. On the other hand, the acoustic mode using CFD mean field inputs results longer than the one based on experimental data. The previous temperature explanation is also applicable for this operational point.

Because of the similarity of the remaining operational points in comparison to the discussed ones, these are not explicitly included. Previously, the frequencies were predicted to be smaller for the linear stability analysis using the CFD simulations as inputs than the frequencies employing experimental data. In Tab. 5.2 this forecast can be checked. Despite the discrepancy, the difference between the frequencies calculated with both methods is smaller than a 5%.

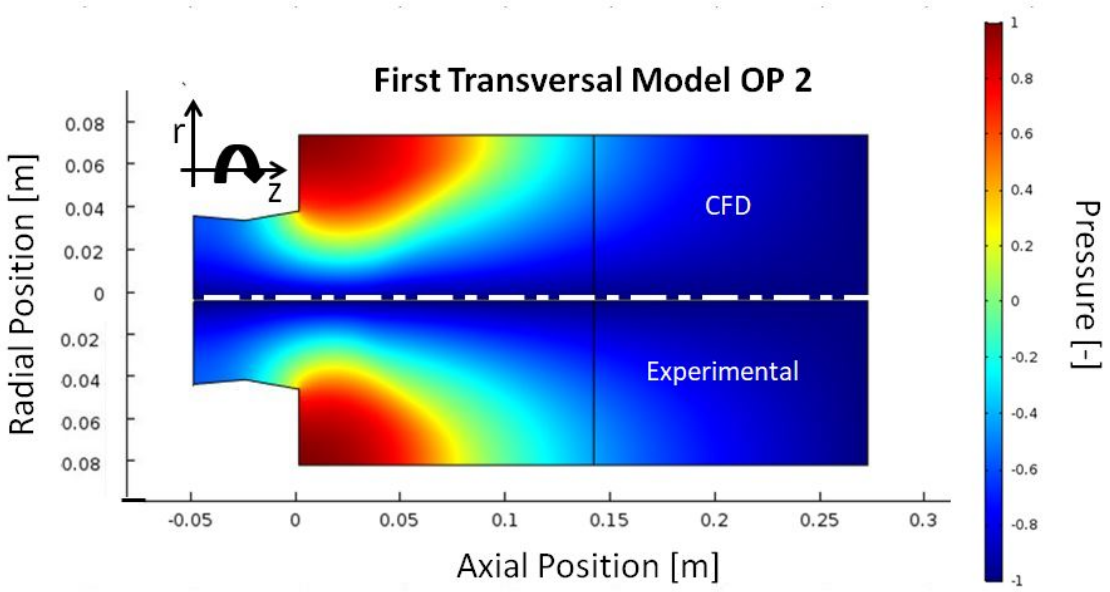

Figure 5.3: Amplitude distribution of fluctuating pressure at the first transversal eigenmode for the reactive case OP 2.

Table 5.2: Frequency comparison between the numerical and experimental methods

Mass Flow [$\frac{g}{s}$]	λ [$\frac{kg_{air,mixuture}}{kg_{air,stoch.}}$]	Frequency Experimental [Hz]	Frequency CFD [Hz]	Difference [%]
80	1.8 (Leaner)	2679	2573	-3,97%
	1.2 (Richer)	2895	2747	-5,08%
120	1.8 (Leaner)	2652	2585	-2,53%
	1.2 (Richer)	2851	2737	-4,00%

The next step is presenting the chamber Rayleigh's indices based on the Rayleigh's criterion, the concept is introduced in Sec. 2.2. Fig. 5.4 displays the total driving rate interaction owned to both displacement and deformation. The Rayleigh's indices indicate the local interaction between the acoustic pressure mode and the unsteady heat release rate. It is a measure of the amount of combustion energy transfer into the acoustic mode. This FEM does not account for damping effects (i.e. thermo-viscous losses or vortex shedding). Therefore, the interaction is expected to contribute to an oscillation amplitude growth (ie. positive driving rate).

However, the Rayleigh's indices show locally different phases between p' and q', resulting into different signs (blue and yellow areas). This means, that the negative sign (yellow) contribution acts as a damping effect[2]. In [13] was discovered that the change in oscillation am-

[2]For the sign convection cf. Sec. 3.4

plitude due to a thermoacoustic instability does not affect the driving rate. To explain this phenomena [13] proposes:

- An amplitude dependent acoustic damping.
- A modal energy transfer because of non-linear acoustics.

From the observation of Fig. 5.4 a hypothesis to explain a linear amplitude dependent damping arises. An increase in the acoustic interaction (i.e. an unstable thermoacoustic behaviour) leads to changes in the flame deformation and displacement, which produces stronger flame motions. This variation may shift the phase difference between p' and q' augmenting the damping. Consequently, the phase shift maintains a constant driving.

In the experimentally obtained Rayleigh's indices (cf. Fig. 5.4), this two zones are differentiated. The region contributing to the amplitude increase, coloured in blue, has a larger importance than the damping zone (yellow). Therefore, the expected driving rate is positive so that the oscillating amplitude increases. The thicker flame [3] in the experimental images permits a clearer observation of this effect than with the CFD reactive simulation. This thicker reaction zone in the experimental method explains why the interaction region is also wider with the experimental data than employing the CFD simulations. However, the contribution to a positive driving rate in the FEM with CFD simulated mean fields is also bigger than the counterphase damping effects. This involves that a positive total driving is expected in both cases. The closer location of the in-phase, positive Rayleigh's indices to the maximum acoustic pressure in both cases is responsible of these positive driving rates.

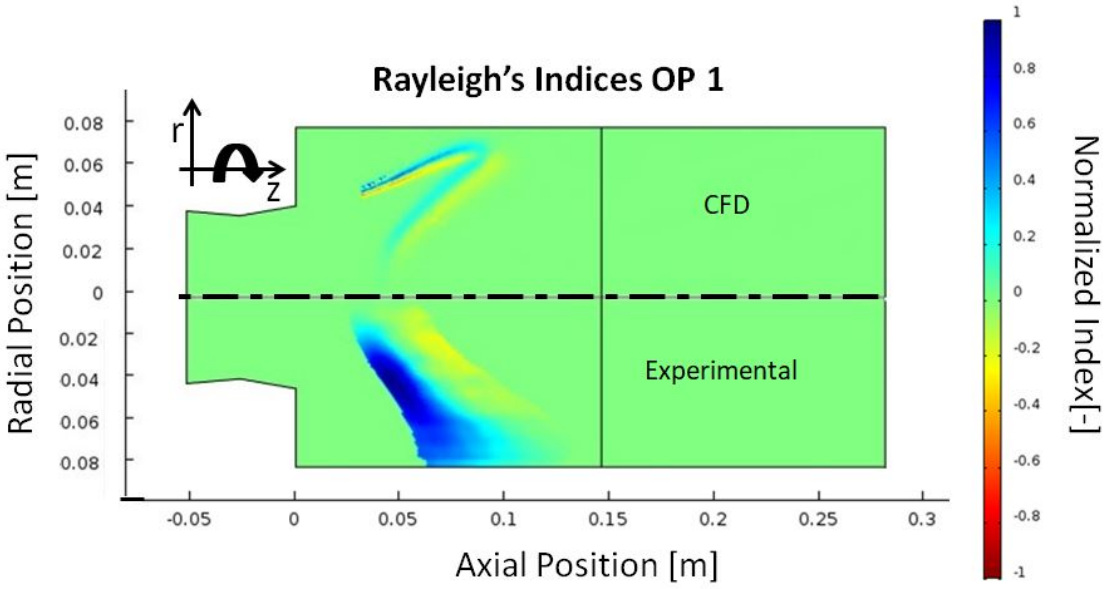

Figure 5.4: Evaluation of the Rayleigh's Indices q' p'. (OP 1)

[3] For the reasons why the experimental flame is thicker see Sec. 4.5

Apart from the thickness difference between both cases, the CFD simulations do not eliminate completely the shear layer burning. This provokes the second contrast, the CFD simulations provide a solution in which the shear layer also presents a thermoacoustic interaction. A priori, whether this shear layer burning causes a higher driving rate is unknown: On the one hand, the shear layer interaction occurs closer to the maximum acoustic pressure so that the contribution to the driving rate is bigger. On the other hand, the counterphase thermoacoustic damping is supposed to be also stronger than in the experimental case as it is also closer to this maximum modal pressure. Despite this uncertainty, it can be forecast that it will yield deviations between the methods.

Another observation that explains a mismatch between the driving rates is the acoustic affected experimental flame. The thermoacoustic interaction enforces the flame heat release rate maximum to be more centred[4]. This variates the position where the thermoacoustic interaction due to deformation occurs. From Fig. 5.4, it can be inferred that the driving rate position is located more centred for the experimental flame. However, the total driving rate because of this effect should not be affected [13]. Tab. 5.3 classifies the phenomena observed with both methods depending on its physical accuracy.

Table 5.3: Comparison between the facts matching and mismatching reality and model for both methods

Method to extract the mean fields	Match the model and reality	Mismatch the model and reality
CFD Simulations	No acoustic interaction	Shear layer burning
	Thin reaction zone	
Experimentation	No shear layer burning	Acoustic interaction in the flame
		Thick reaction zone

Finally, the resulting driving rates are shown and compared. Fig. 5.5 (left) displays the total driving rate. It reveals a small deviation to the experimentally based counterparts. The relative errors for the total driving rate are smaller than 15% for the OP 3 and they don't exceed a 8% error in the rest of the cases. However, the right part of Fig. 5.5 represents the deformation and displacement driving rates, which exhibit a higher discrepancy.

According to [13], the components of the driving rates deviation compensate the variations of the thermoacoustic oscillation amplitudes. As it is explained in Fig. 5.4, the acoustically affected experimental flame delivers a more centred heat release rate distribution. That may be the reason explaining the deformation part difference, the CFD extracted flame shows a higher deformation component because its heat release rate fluctuation is closer to the maximum modal pressure. However, this discrepancy in deformation is compensated by the displacement driving rate. In fact, the CFD flame displacement component shows negative value which involves a damping character. As it was discussed previously, the damping with this STF is caused by a counterphase $p' - q'$ interaction.

[4] See Figs. 4.12 and 4.11 in Sec. 4.5

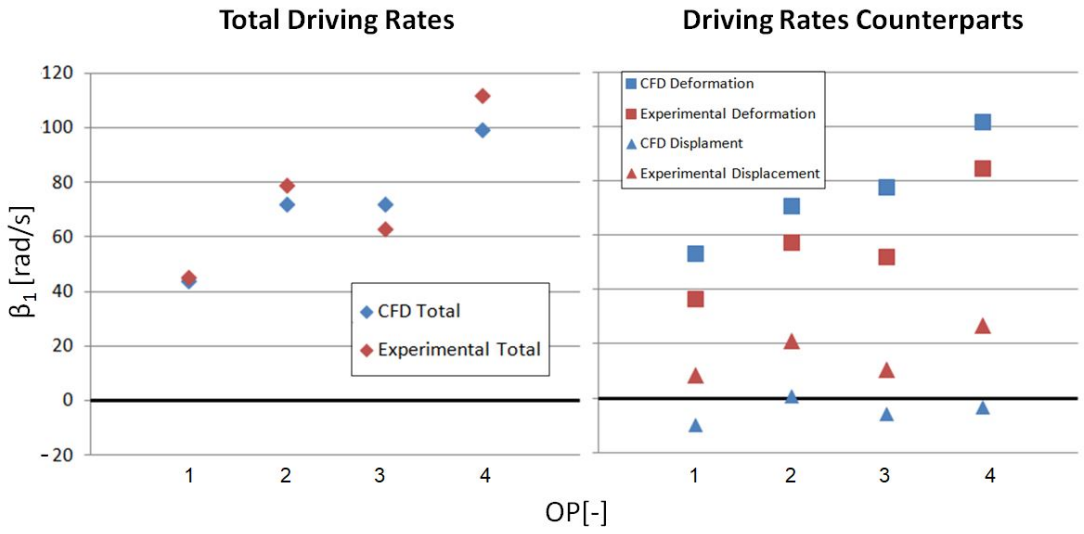

Figure 5.5: Total driving rates (left) and their counterparts (right)

6 Summary and Conclusions

The FEM implementation of an available STF allowed to quantify the impact of the heat release rate fluctuations on the driving rates of the first transversal acoustic mode in a swirl stabilized combustor. Specifically, this STF accounts for fluctuations associated with the flame displacement and deformation, provoked by acoustic interactions.

This Bachelor's thesis is motivated by the necessity of determining the mean temperature and heat release rate fields without acoustic interaction to fulfil the STF requirements. Due to the unfeasibility of removing the acoustic interaction from the experimental flames, the use of a steady-state CFD simulation to reproduce an acoustics free flame arises. Derived benefits from the CFD simulation with respect to experiments (e.g. costs and time reduction) make this procedure more interesting.

A procedure to emulate the flame is implemented by steady-state CFD simulations. The method comprises of an isothermal CFD simulation of the complete combustor configuration that enables to determine the turbulence and mean velocity fields in the combustion chamber inlet. These profiles are employed as an inlet boundary to perform a reactive CFD simulation of the combustion chamber. The use of an extended version of the FGM flame model delivers a reduction in the shear layer burning. The numerically extracted mean temperature and heat release rate are compared to the experimentally obtained.

A linear stability analysis with the numerical mean fields as an input is conducted. The results are compared with the driving rates which were obtained using experimental inputs to validate the CFD procedure.

The conclusions extracted from this work are:

- The steady-state CFD simulations show a good agreement with the experimental OH* data.
- The total driving rates based on CFD data reveal an accurate match with the experimentally based date.
- The displacement and deformation components present the biggest difference. However, this mismatch was expected due to the lack of acoustic effects in the CFD simulations.

Therefore, the method can be used to predict thermoacoustic instabilities, without the ne-

cessity of experimentally determining the mean temperature and heat release rate fields. The following further work is proposed using the developed procedure as a tool:

- The experimental data of extra operational points is available. Therefore, the linear stability analysis of the first transversal mode can be completed.
- Driving rate calculation of the second transversal mode. Since this procedure shows acceptable accuracy for the first transversal mode, it can be applied to others modes of interest in combustors.
- This procedure neglects damping effects. Therefore, the inclusion of a model quantifying the acoustic damping caused by vortex shedding in the shear layer is necessary.
- The flame shape is a decisive factor in the final results of this procedure. In order to improve them it is recommended to eliminate the burning in the shear layer.
- An investigation the phase shift between q' and p' depending on the oscillation amplitude increase. This may discover a explanation for the findings in [13] without accounting for non-linear phenomena.

List of Figures

List of Tables

Bibliography

[1] *COMSOL 5.2. User Guide*, 2015.

[2] *Fluent 18.0. Theory Guide.*, 2017.

[3] *Fluent 18.0. User's Guide*, 2017.

[4] Energy International Agency. Anual energy report, 2017.

[5] Energy International Agency. Emissions tools and faq, 2017.

[6] A.Torregrosa. *Fundamentos de Termodinámica*. UPV, 2015.

[7] BP. Statistical review of world energy, 2017.

[8] J. de la Morena and P.Piqueras. *Propulsión*, chapter Gas Turbines Cycles. UPV, 2016.

[9] D. Dunn-Rankin and P.Therkelsel. *Lean Combustion Technology and Control*. Academic Press, 2016.

[10] F. Berger el al. High-frequency thermoacoustic modulation mechanisms in swirl-stabilized gas turbine combustors, part one: Experimental investigation of local flame response. In *ASME Turbo Expo 2016 GT2016-57583, June 13-17, Seoul, South Korea.*, 2016.

[11] F. Berger et al. High-frequency thermoacoustic modulation mechanisms in swirl-stabilized gas turbine combustors, part two: Modelling and analysis. In *ASME Turbo Expo 2016 GT2016-57583, June 13-17, Seoul, South Korea.*, 2016.

[12] F. Berger et al. Extraction of linear growth and damping rates of high-frequency. In *ASME Turbo Expo 2017 GT2017-64233 June 26-30, Charlotte, NC, USA*, 2017.

[13] F. Berger et al., editor. *Pulsation-Amplitude-Dependent Flame Dynamics of High-Frequency Thermoacoustic Oscillations in Lean-Premixed Gas Turbine Combustors*. ASME, April 2018.

[14] N. Klarmann et al. Impact of flame stretch and heat loss on heat release distributions in gas turbine combustors: Model comparison and validation. In *ASME Turbo Expo 2016, GT2016-57625, June 13-17, Seoul, South Korea*, 2016.

[15] J.H. Ferziger and Peric M. *Computational Methods for Fluid Dynamics*. Springer, Berlin, 2002.

[16] V. Gummer. *Flugantriebe I und Gasturbinen*, chapter Overview of Engines. TUM, 2017.

[17] C. Hirsch. *Technische Verbrennung Einführung in Theorie und Anwendungen technischer Verbrennungsysteme*. TUM, 2015.

[18] A. Hirschberg and S.W. Rienstra. *An Introduction to Acoustics*. Eindhoven University of Technology, 2016.

[19] H.J.Kaltenbach. *Aeroakustik*, chapter Grundlagen. TUM, 2017.

[20] J.M.Desantes. *Fenómenos de Transporte de Masa y Energía*, chapter Transporte de la Cantidad de Movimiento. UPV, 2016.

[21] N. Klarmann and T. Sattelmayer. Flamelet generated manifolds for partially premixed, highly stretched and non-adiabatic combustion in gas turbines. Technical report, American Institure of Aeronautics and Astronautics, 2016.

[22] T. Lieuwen. *Unsteady Combustor Physics*. Cambridge University Press, 2012.

[23] United Nations. Demographic forecasts.

[24] P.Martí and R.Navarro. *Ampliación de Mecánica de Fluidos*, chapter Preproceso en CFD. UPV, 2016.

[25] J. Seebold. *Combustion Handbook*. IFRF, 2005.

[26] Siemmens. Products overview, 2018.

[27] V.Gummer. *Flugantriebe I und Gasturbinen*, chapter Combustion Basics and Emissions. TUM, 2017.

[28] V.Gummer. *Turbomaschinen*, chapter Prozessführung GT Anlagen. TUM, 2018.

[29] W.Erhard. *Flugantriebe 2*, chapter Anbau- und Hilfsysteme. TUM, 2018.